APPENDIX B

DYNAMIC RESPONSE OF PILES TO EARTHQUAKE LOADING—ANALYTICAL

INTRODUCTION

Catastrophic damage resulting from recent earthquakes has raised concerns about the current codes and approaches used for the design of structures and foundations. In the past, free-field accelerations, velocities, and displacements have been used as input ground motions for the seismic design of structures without considering the kinematic interaction of the foundation or the site effects that have resulted from the soil stratigraphy and the introduction of piles. Depending on the pile or pile group configuration and soil profile, free-field response may underestimate or overestimate actual in situ conditions that will result in radically changed foundation and structural behavior and, therefore, in impact design criteria.

The behavior of pile foundations during an earthquake event is influenced by the interaction of the pile foundation with the surrounding soil medium. This interaction can be categorized into (1) kinematic interaction and (2) inertial interaction. The former characterizes the response of piles to the seismic loading through the soil; the latter describes the pile-soil interaction caused by the inertial loading from the superstructure applied at the pile head. The characteristics of the pile-soil interaction in these two types of loading are different; therefore, the kinematic interaction and the inertial interaction are addressed separately.

KINEMATIC RESPONSE OF PILES

Recent destructive earthquakes have highlighted the need for increased research into the revamping of design codes and building regulations to prevent further catastrophic losses in terms of human life and economic assets. The present study investigated the response of single piles to kinematic seismic loading using the three-dimensional finite element program ANSYS (*1*).

The objectives of this study were twofold:

1. Develop a finite element model that can accurately model the kinematic soil-structure interaction of piles, accounting for the nonlinear behavior of the soil, discontinuity conditions at the pile-soil interface, energy dissipation, and wave propagation.
2. Use the developed model to evaluate the kinematic interaction effects on the pile response with respect to the input ground motion. The results of a number of studies on the kinematic interaction of pile groups reported in the literature are also included.

Assumptions and Restrictions

The problem to be addressed is shown in Figure B-1. As shown, the actual system consists of a pile foundation supporting a typical bridge pier. Current design codes use the free-field motion as the input ground motion at the foundation level. The analysis described herein attempted to evaluate the interaction of the pile-soil system and how it alters the free-field motion and modifies the ground motion at the foundation level.

The dynamic loading was applied to the rigid underlying bedrock (see Figure B-1) as one-dimensional horizontal acceleration (X-direction in finite element model), and only horizontal response was ascertained. Vertical accelerations were ignored because the margins of safety against static vertical forces usually provide adequate resistance to dynamic forces induced by vertical accelerations. Wu and Finn (*2*), using a three-dimensional elastic model, found that deformations in the vertical direction and normal to the direction of shaking are negligible compared with the deformations in the direction of horizontal shaking.

Although the finite element analysis used in this study includes important features such as soil nonlinearity and gapping at the pile-soil interface, it does not account for buildup of pore pressure because of cyclic loading. Thus, neither the potential for liquefaction nor the dilatational effect of clays and the compaction of loose sands in the vicinity of piles is accounted for in the current analysis. Furthermore, the inertial interaction between the superstructure and the pile-foundation system is not considered here. The analysis is limited to the response of free-headed piles with no external forces from the superstructure ("D'Alembert forces") to understand better the kinematic interaction effects in seismic events.

Three-Dimensional Finite Element Model

Model Formulation

Full three-dimensional geometric models were used to represent the pile-soil systems. Exploiting symmetry, only one-half of the actual model was built, thus significantly reducing computing time and cost. Figure B-2 depicts the pile-soil system considered in the analysis, showing an isometric view of the half of the model used. Figures B-2 and B-3 show the finite element mesh (Mesh No. 3) used in the analysis.

The pile and soil were modeled using eight-noded block elements. Each node had three translational degrees of freedom (i.e., *X*, *Y* and *Z* coordinates), as shown in Figure B-4. A three-

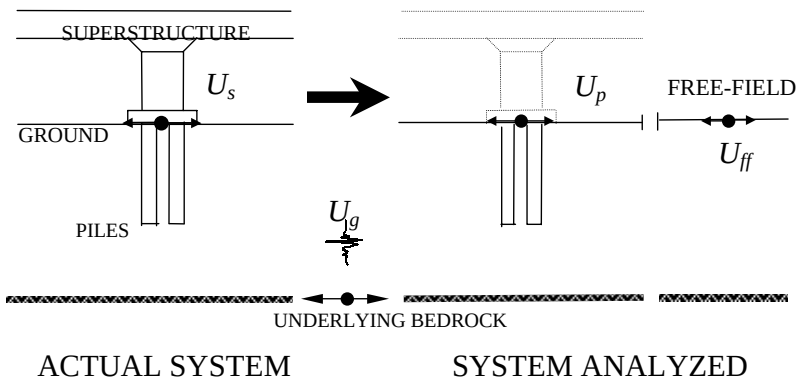

Figure B-1. Definition of the problem and terminology (actual acceleration, U_s*; acceleration due to kinematic interaction only,* U_p*; bedrock acceleration,* U_g*; and free-field acceleration,* U_{ff}*).*

dimensional point-to-surface contact element was used at the pile-soil interface to allow for sliding and separation in tension, but ensured compatibility in compression. The contact element had five nodes with three degrees of freedom at each node (i.e., translations in the *X*, *Y* and *Z* directions), as shown in Figure B-4b. Transmitting boundaries were used to allow for wave propagation and to eliminate the "box effect" (i.e., the reflection of waves back into the model at the boundaries) during dynamic loading. The element used to model the transmitting boundary consisted of a spring and a dashpot arranged in parallel, as illustrated in Figure B-4c.

Soil Properties

To evaluate the effect of soil plasticity on the pile response, the soil was modeled using two approaches: a homogeneous elastic medium and an elastoplastic material using the Drucker–Prager failure criteria. For cases involving plasticity, the angle of dilatancy was assumed to be equal to the angle of internal friction (associated flow rule). There was no strain hardening; therefore, no progressive yielding was considered. Because pore pressures were not considered in this

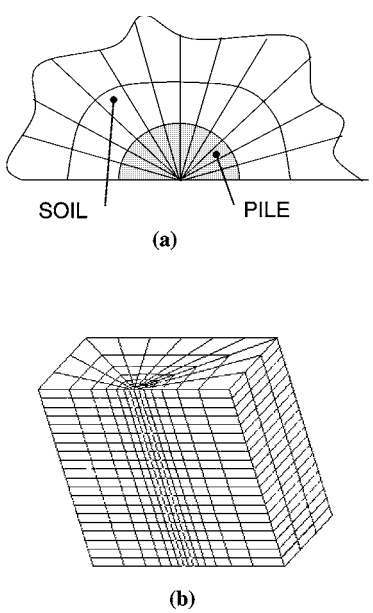

Figure B-2. Pile-soil system. (a) Detail of wedge-shaped pile elements surrounded by soil elements (plan view). (b) Isometric view of soil and pile mesh model.

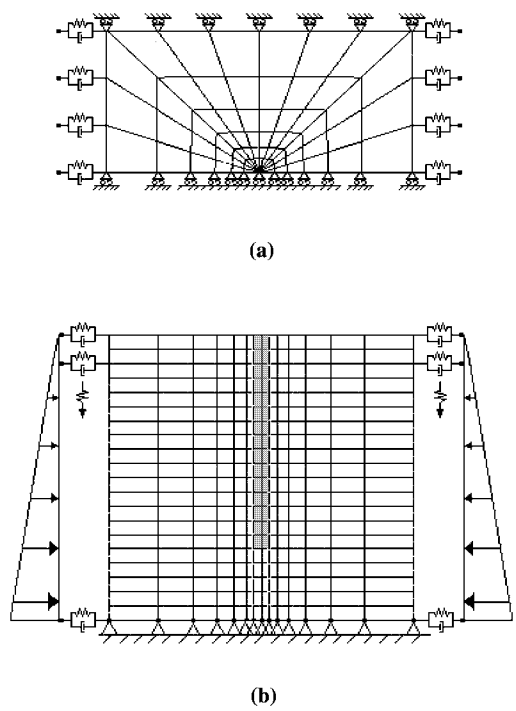

Figure B-3. Finite element mesh (Mesh No. 3) showing boundary conditions. (a) Plan view. (b) Front cross-section view with geostatic pressure distribution.

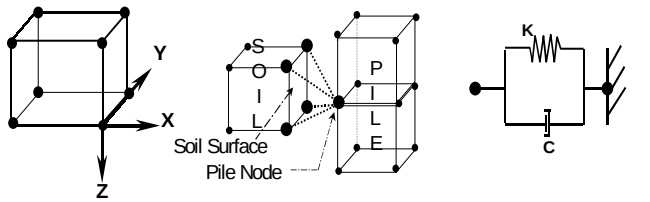

(a) - 8 noded block element, DOF: X, Y, Z **(b) - 5 noded contact element, DOF: X, Y, Z** **(c) - 2 noded boundary element, DOF: X, Y, Z**

Figure B-4. Soil and pile model elements: (a) block element used for soil and pile; (b) surface contact element used between pile and soil to allow for slippage and separation; (c) transmitting boundary element consisting of "spring(K)" and "dashpot(C)" to allow for radiating boundaries.

analysis, effective stress parameters and drained conditions were assumed. The material damping ratio of the soil, β, was assumed to be 5 percent (i.e., $D = 10$ percent). This soil material damping ratio is compatible with the expected strain level under earthquake loading. The governing equations of the system are given by

$$[M]\{\ddot{u}\} + [C]\{\dot{u}\} + [K]\{u\} = \{F(t)\}, \qquad \text{(B-1)}$$

where $\{\ddot{u}\}$, $\{\dot{u}\}$, and $\{u\}$ are the acceleration, velocity and displacement vectors, respectively, and $[M]$, $[C]$, and $[K]$ are the global mass, damping, and stiffness matrixes. The damping matrix is given by $[C] = \zeta\,[K]$, in which the damping coefficient, ζ, is $2\beta/\omega_0$, and ω_0 is the predominant frequency of the loading (rad/s). Material damping was assumed to be constant throughout the entire seismic event, although the damping ratio varies with the strain level.

Pile Properties

Cylindrical reinforced concrete piles with linear elastic properties were considered in this study. The piles were modeled using eight-noded brick elements. The cylindrical geometry was approximately modeled using wedge-shaped elements (see Figure B-2a). No damping was considered within the piles, and relevant parameters are listed in Figure B-5.

Pile-Soil Interface

Modeling of the pile-soil interface is crucial because of its significant effect on the response of piles to lateral loading (*3*). Two cases were considered in the analysis:

1. The pile and soil were perfectly bonded, in which case the perimeter nodes of the piles coincided with the soil nodes (elastic with no separation).
2. The pile and soil were connected by frictional interface elements that are described below.

The contact surface (i.e., the pile) is said to be in contact with the target surface (i.e., the soil) when the pile node penetrates the soil surface. A very small tolerance was assumed to prevent penetration and to achieve instant contact as pile nodes attempt to penetrate the soil nodes (or vice versa). Coulomb friction was employed between the pile and soil along the

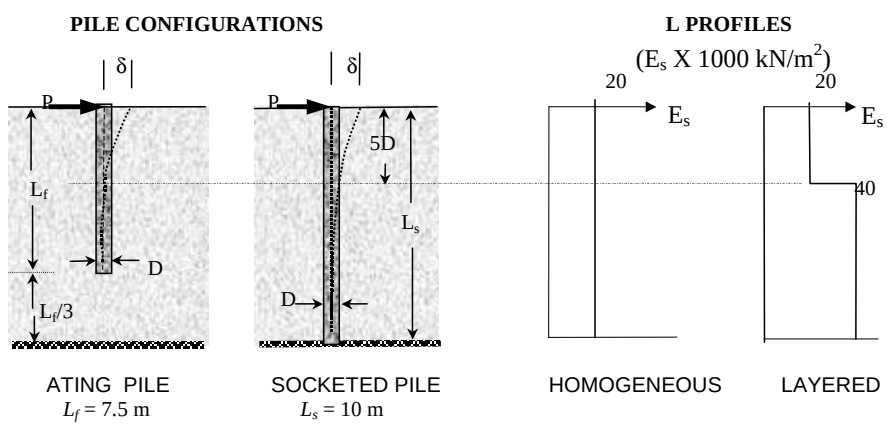

E_s= Soil Young's Modulus
δ = Horizontal deflection
P = Horizontal load
V_s = Shear wave velocity = 60-120 m/s
c' = 34 kPa, $\phi = \Psi = 16.5°$ (Plasticity)

E_p= Pile Young's Modulus = $2*10^7$kPa
ρ_s = Soil submerged unit weight = 11.8 kN/m^3
ρ_p = Pile mass density = 2.3 Mg/m^3
ν_s = Soil Poisson's ratio = 0.45
ν_p = Pile Poisson's ratio = 0.30

Figure B-5. Two-dimensional representation of floating and socketed pile in either homogeneous (used for verification) or layered soil profile.

entire pile length as well as to the pile tip (for floating piles). The coefficient of friction relating shear stress to the normal stress was chosen according to American Petroleum Institute (API) recommendations (*4*) and was assumed to be 0.7. The contact surface coordinates and forces were fully updated to accommodate any large or small deflections that may occur. The penalty function method was used to represent contact with a normal contact stiffness (K_n). K_n allowed the interface element to deform elastically before slippage occurred and was chosen to be equal to the shear modulus of the soil. Convergence was achieved, and over-penetration was prevented using K_n = 6800 kN/m (numerically equal to the shear modulus of the soil).

Boundary Conditions

Boundary conditions varied depending on the type of loading. For static loading, the bottom of the mesh (representing the top of the bedrock layer) was always fixed in all directions. All symmetry faces were fixed against displacement normal to the symmetry plane, but were free to move on the surface of the plane. The nodes along the top surface of the mesh were free to move in all directions. The nodes along the sides of the model were free to move vertically, but were constrained in the horizontal direction by a Kelvin element in order to represent a horizontally infinite soil medium during static and dynamic analyses. The constants were calculated using the solution due to Novak and Mitwally (*5*), given by

$$k_r = \frac{G}{r_0}\left[S_1(a_0, \nu, \zeta) + iS_2(a_0, \nu, \zeta)\right], \qquad \text{(B-2)}$$

where

k_r = total stiffness,
G = soil shear modulus,
r_0 = distance to finite element boundary,
S_1 and S_2 = dimensionless parameters from closed form solutions,
ν = Poisson's ratio,
a_0 = dimensionless frequency equal to $r_0\omega/V_s$,
ω = circular frequency of loading, and
V_s = shear wave velocity of the soil.

The real and imaginary parts of Equation B-2 represent the stiffness (K) and damping (C), respectively, that is

$$K = \frac{GS_1}{r_0} \text{ and } C = \frac{GS_2}{\omega r_0}. \qquad \text{(B-3)}$$

To determine the stiffness and damping of the Kelvin elements, the constants given in Equation B-3 were multiplied by the area of the element face (normal to the direction of loading) because they assume constant unit area of contact. For static loading (i.e., zero frequency), the damping term vanishes, and the element reduces to a spring only.

For dynamic loading, ω was taken as the predominant frequency of the earthquake load and was determined from a discrete Fourier transform of the time history of the input motion. Figure B-6 shows the Fourier amplitude (c_n) versus frequency (ω_n) content for the strong motion record used in the study. It is evident that a narrow spectrum exists at a dominant frequency of approximately 2 Hz.

Time-dependent displacements were applied to the stratum base to simulate seismic loading. All other boundary conditions remained unchanged and are portrayed in Figure B-3.

Loading Conditions

Initial Loading

The state of stress in the pile-soil system in actual in situ conditions was replicated as an initial loading condition prior to any additional dynamic or static external load. That is, geostatic stresses were modeled by applying a global gravitational acceleration, *g*, to replicate vertically increasing stress with depth. A linearly increasing pressure with depth was applied to the periphery of the soil block to replicate horizontal stresses as shown in Figure B-3b. A coefficient of lateral earth pressure, K_o = 0.65, typical of many geological conditions, was used. Because of the difference in density and stiffness for the pile and soil, the soil tended to settle more than the pile in the vertical direction, resulting in premature slippage at the pile-soil interface. To eliminate this false representation of initial conditions, the difference between the relative displacement between the soil and the pile was accounted for by adding

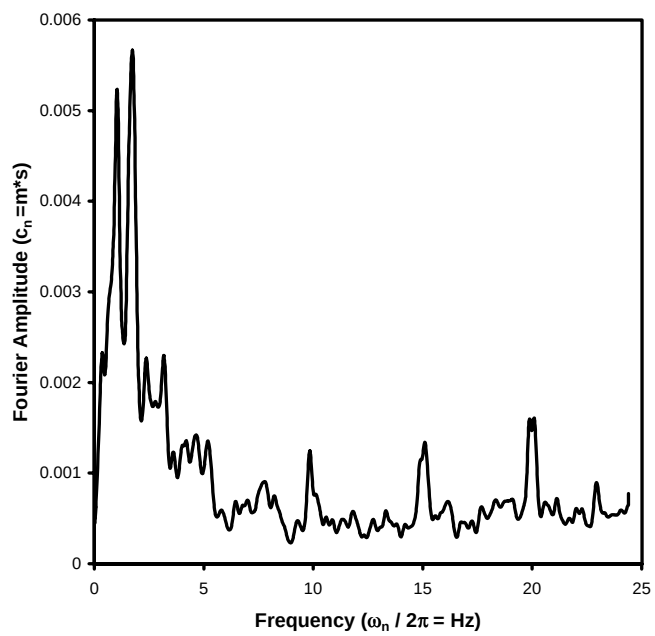

Figure B-6. Fourier amplitude spectrum for earthquake loading at the bedrock level.

a corresponding body load to the pile. The resulting mesh represented in situ conditions, especially for drilled shafts.

Static Loading

All static loads were applied as distributed loads along the perimeter of the pile head that was level with the ground surface. Only one-half of the total load was applied to the pile in the finite element analysis because of the symmetric geometry of a full circular pile.

Dynamic Loading

Strong motion records from the 1989 Loma Prieta earthquake in California ($M_L = 7.1$) were used in the finite element study. The accelerogram and displacement data used were from the Yerba Buena Island rock outcrop station in Santa Cruz Mountain (*6*). The measured displacements were applied to the top of the rigid bedrock layer at 0.02-s intervals. Considering that the maximum acceleration of the measured one-dimensional motion was 0.03 g, the accelerations were multiplied by a factor of seven to simulate a PHA (peak horizontal acceleration) of approximately 0.2 g for the bedrock input motion. It is important to note that the acceleration data were for bedrock motions and not for free-field motions that can either increase or decrease in terms of PHA because of the site effects. Motions of a 20-s duration were modeled to include all of the important features of the earthquake. The predominant frequency was approximately 2 Hz, which is typical of destructive earthquakes (*7*).

Verification of the Finite Element Model

The verification process followed incremental steps to ensure that pile, soil, and boundary conditions were separately accounted for in order to minimize error accumulation. The size of the mesh was mainly dependent on the loading conditions (static or dynamic) and geometry of the piles. The mesh was refined near the pile to account for the severe stress gradients and plasticity encountered in the soil, with a gradual transition to a coarser mesh away from the pile in the horizontal *X* and *Y* directions. The vertical *Z*-direction subdivisions were kept constant to allow for an even distribution of vertically propagating SH-waves. The maximum element size, E_{max}, was less than one-fifth to one-eighth of the shortest wavelength (λ) to ensure accuracy (*7*), that is,

$$E_{max} < (1.5 - 1.8) \times \lambda, \qquad \text{(B-4)}$$

where λ is V_s/f, V_s is the soil shear wave velocity, and f is the excitation frequency in Hz. The minimum V_s was 60 m/s, and the dynamic loading had a cut-off frequency equal to 20 Hz. Thus, a maximum element length of 0.5 m was adopted.

The proposed element division was verified using results from a sensitivity study focussing on vertical pile shaft discretization by El Sharnouby and Novak (*8*), who found that using 12 to 20 elements gave accurate results with a minimum of computational effort. Thus, that range was adopted for this study.

The pile mesh was first verified by considering the pile as a fixed cantilever in air (no soil). Lateral deflections resulting from a static load for three different pile mesh sizes were compared with one-dimensional beam flexure theory, and the maximum difference was 8 percent. The results were very close; the small differences, however, could be explained by the fact that beam theory is not exact (it ignores shear deformations), and the finite model was not a perfect cylinder. Since the maximum number of elements (6,000) and nodes (11,000) available was limited, 180 elements were used to model the pile (accuracy within 8 percent of theoretical solutions). When soil and boundary elements were added, the total number of elements was close to the limit.

The soil was added to the model assuming a homogeneous soil stratum (see Figure B-5). The elastic responses of socketed and floating single piles in the homogeneous soil stratum were compared with the results from two different analyses: (1) the results from Poulos and Davis (*9*) using Mindlin's equations and enforcing pile-soil compatibility; and (2) the results presented by Trochanis et al. (*3*) using a three-dimensional finite element analysis, although their pile had a square cross section but the same flexural rigidity. Three different soil meshes were built with increasing refinement to determine an acceptable level of accuracy while maintaining a computationally efficient model. Mesh No. 1 consisted of 1,080 elements, Mesh No. 2 consisted of 2,640 elements, and Mesh No. 3 had 3,280 elements. Other meshes with a total number of elements equal to 6,000 were also tested, but were not used because of unreasonable computer processing time.

The results for the linear elastic response under lateral loading at the pile head are shown in Figure B-7a. The mesh that yielded the closest match (Mesh No. 3, depicted in Figures B-2 and B-3) was used in the analysis. The deflections obtained in this study were slightly greater than those from Poulos and Davis (*9*). However, those authors pointed out that their solution might underestimate the response of long piles in soft soils. Figures B-7b and B-7c show pile-head deflections considering separation at the pile-soil interface and soil plasticity, respectively. It can be seen that good agreement exists with the results from Trochanis et al. (*3*). The differences in the plastic soil case may be attributed to the use of a different model for soil plasticity (a modified Drucker–Prager model). Figures B-8a and B-8b show the elastic soil surface displacements away from the pile compared with results from elastic theory by Poulos and Davis (*9*) and other finite element analyses (*3*). It can be seen from Figures B-8a and B-8b that the results obtained using Mesh No. 3 agree well with both solutions, especially close to the pile. The pressure distribution in the soil agreed equally well.

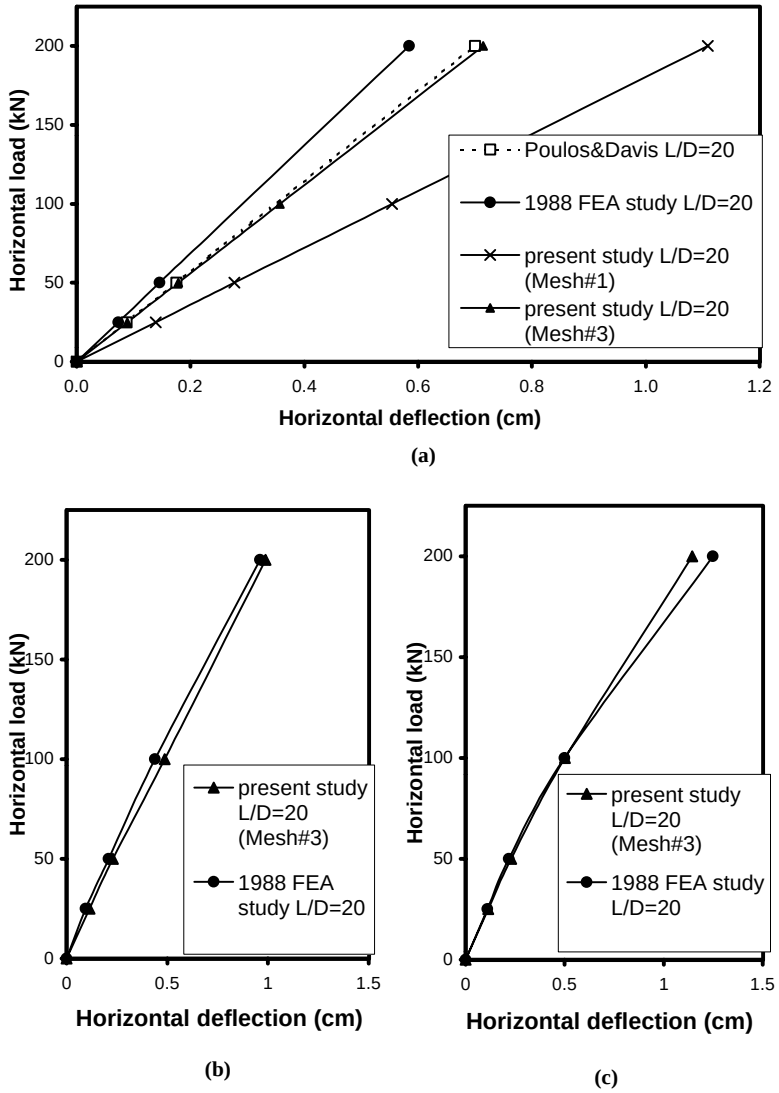

Figure B-7. Response of single socketed pile for (a) elastic, (b) elastic-gapping, (c) plastic-gapping.

The final step in the verification process was accomplished by solving the ground response to an earthquake signal using the finite element model and comparing the elastic free-field response with that obtained using the program SHAKE91 (*10*). Considering that SHAKE91 is a one-dimensional analysis, constraints were applied to the finite model to allow only displacements in the direction of shaking (1 degree of freedom per node) to replicate one-dimensional results. The results from the finite element analysis and SHAKE91 are plotted in Figure B-9 for elastic response using the same parameters. A constant shear modulus and material damping ratio were used in both the SHAKE91 and the finite element analysis models. It can be seen from Figure B-9 that the agreement is good along the entire time period considered. The maximum free-field accelerations for the finite element analyses and SHAKE91 were amplified to approximately 0.6 g from 0.2 g (bedrock input motion) and are compared with bedrock accelerations in Figure B-10. The same finite element analysis model was modified to allow for three-dimensional response, and the free-field response is plotted against the one-dimensional results in Figure B-11. The maximum free-field acceleration obtained from three-dimensional analysis was only 0.35 g (see Figure B-11). The accelerations calculated from the three-dimensional analysis are closer to those observed during actual seismic events. Hence, it was concluded that the three-dimensional analysis resulted in realistic acceleration magnitudes; therefore, all further models discussed herein assumed full three-dimensional capability.

Numerical Study for Kinematic Interaction

The kinematic effects of piles in a homogeneous soil medium were evaluated by comparing acceleration time histories and Fourier spectra of the pile head and the free-field.

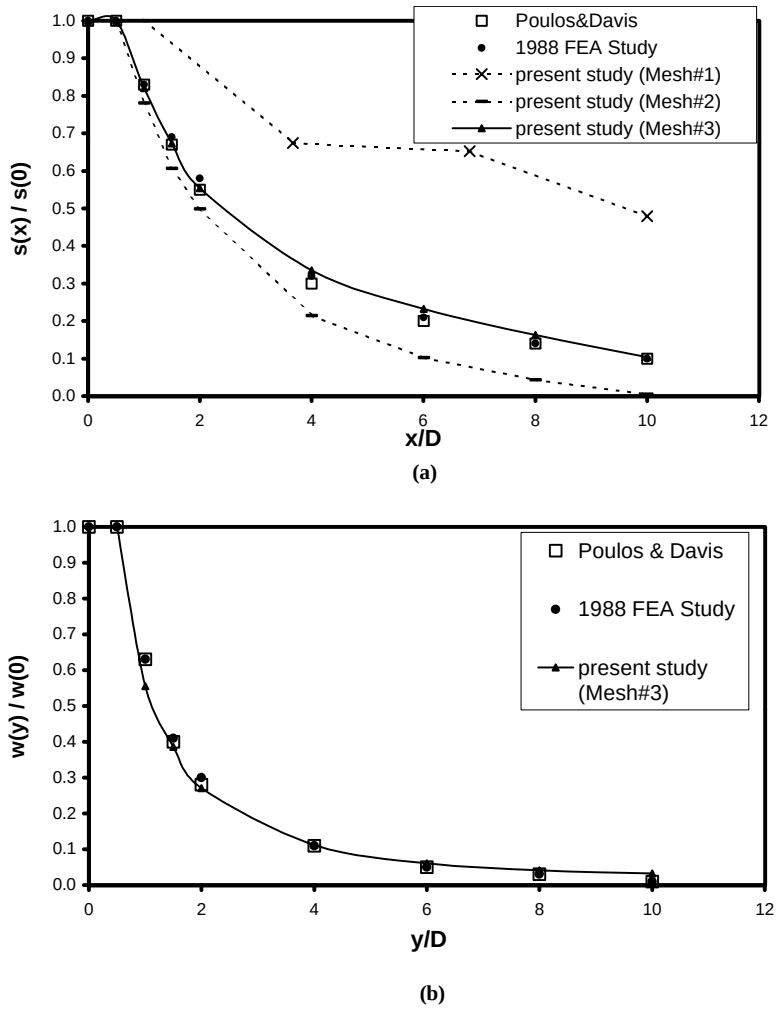

Figure B-8. Elastic soil surface displacements. (a) Comparison of soil displacements' long line of loading, s(x)*, relative to pile-head displacement,* s(0)*. (b) Comparison of soil displacements normal to direction of loading,* w(y)*, relative to pile-head displacement,* w(0)*.*

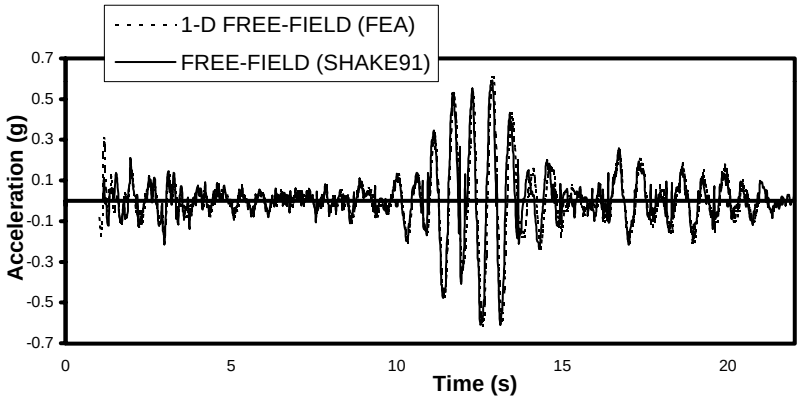

Figure B-9. One-dimensional verification of finite element analysis (FEA using ANSYS) with SHAKE91.

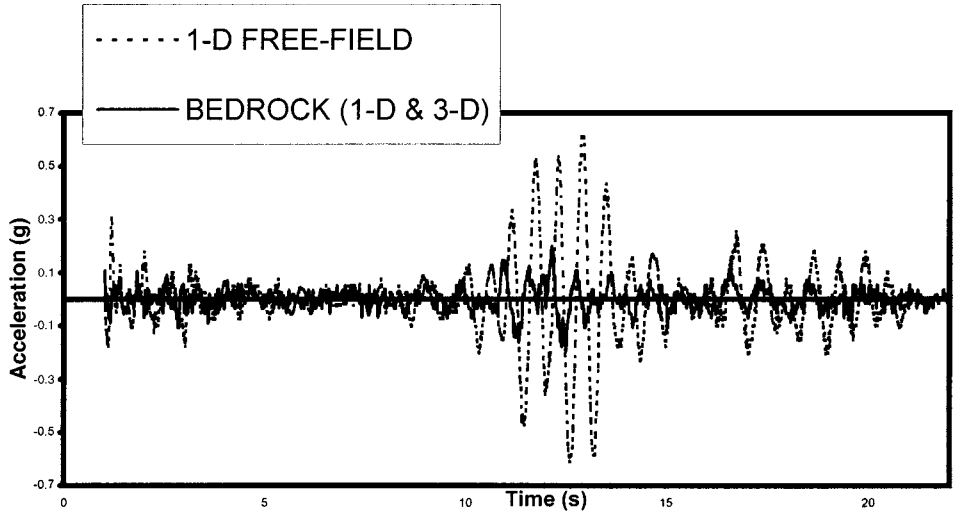

Figure B-10. Response of underlying bedrock and free-field for homogeneous soil (using one-dimensional finite element analysis).

The same dynamic loading was applied in all cases (i.e., Loma Prieta data) to the underlying bedrock for a homogeneous soil profile. Results from seven different pile-soil configurations were obtained and are referred to in Figures B-12 through B-18. The following notation is used throughout the graphs and literature to identify each test case (see Figure B-5 for soil and pile parameters):

- **EFH** (**e**lastic, **f**ree-field, **h**omogeneous)—refers to the free-field response using linear isotropic viscoelastic constitutive relations.
- **PFH** (**p**lastic, **f**ree-field, **h**omogeneous)—refers to the free-field response using a perfect elastic-plastic soil model, Drucker–Prager criteria.
- **ESNFH** (**e**lastic, **s**ingle pile, **n**o separation, **f**loating, **h**omogeneous)—refers to the floating single pile–head response using a linear isotropic viscoelastic soil with no separation at the pile-soil interface, L/D = 15, E_p/E_s = 1,000.
- **ESNSH** (**e**lastic, **s**ingle pile, **n**o separation, **s**ocketed, **h**omogeneous)—refers to the socketed single pile–head response using a linear isotropic viscoelastic soil with no separation at the pile-soil interface, L/D = 20, E_p/E_s = 1,000.
- **ESSFH** (**e**lastic, **s**ingle pile, **s**eparation, **f**loating, **h**omogeneous)—same as the ESNFH case, but allows for separation at the pile-soil interface.
- **PSSFH** (**p**lastic, **s**ingle pile, **s**eparation, **f**loating, **h**omogeneous)—refers to the floating single pile–head response using a perfect plastic-elastic soil model with separation allowed at the pile-soil interface, $L/D = 15$, $E_p/E_s = 1{,}000$, $c' = 34$ kPa, $\psi = 16.5°$.

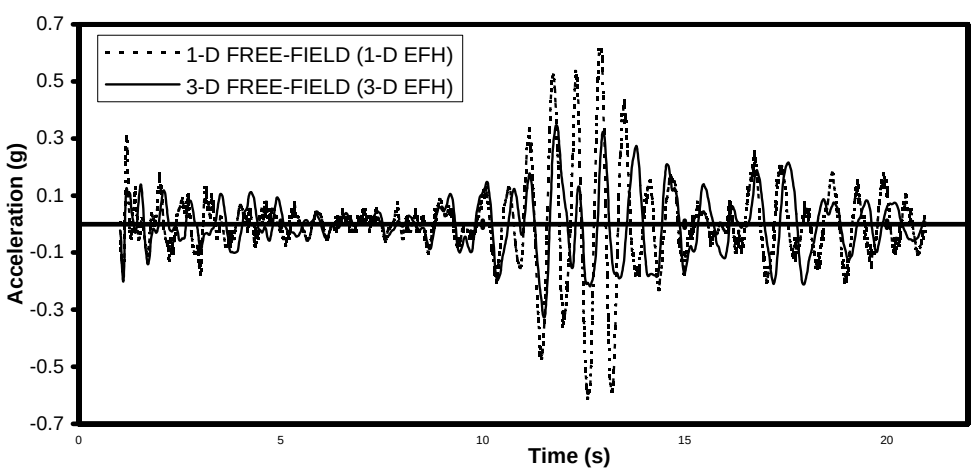

Figure B-11. Elastic free-field response for homogeneous soil (EFH) for one- and three-dimensional analysis.

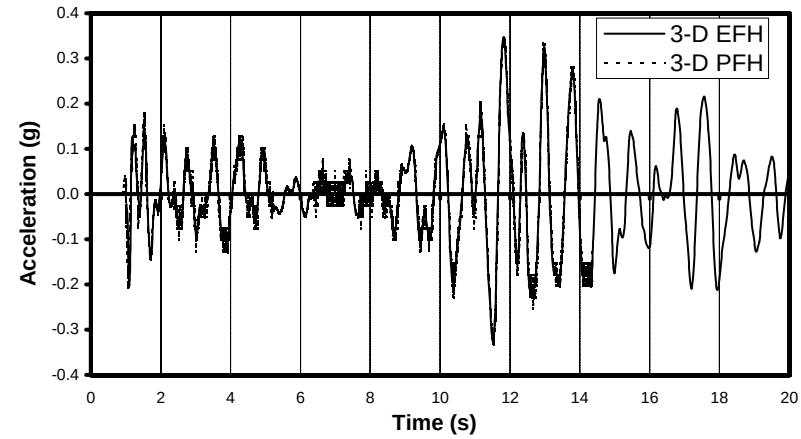

(a)

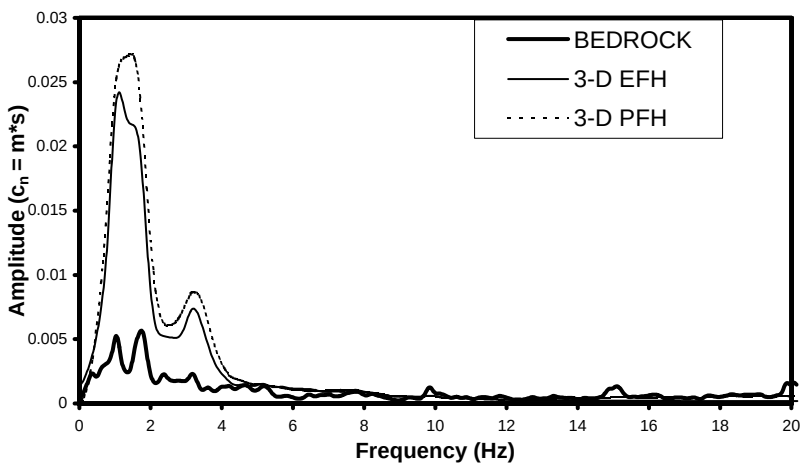

(b)

Figure B-12. Comparisons of the free-field response for the elastic and plastic soil cases and the Fourier spectra for elastic and plastic soil profiles against the input bedrock spectrum. (a) Comparison between calculated accelerations for elastic free-field (EFH) and plastic free-field (PFH) using the Drucker–Prager criteria for a homogeneous soil profile. (b) Fourier spectrum for the response at the bedrock level, elastic soil free-field and plastic soil free-field.

- **PSSSH** (**p**lastic, **s**ingle pile, **s**eparation, **s**ocketed, **h**omogeneous)—refers to the socketed single pile–head response using a perfect plastic-elastic soil model with separation allowed at the pile-soil interface, $L/D = 20$, $E_p/E_s = 1{,}000$, $c' = 34$ kPa, $\psi = 16.5°$.

Results

Figure B-12a compares the free-field response for the elastic and plastic soil cases. The difference between the two cases is not evident over the 20-s duration, but a more detailed evaluation is presented in Figure B-15 for the 2- through 10-s interval. The acceleration response is slightly amplified using a plastic soil model. This can be attributed to the limiting ultimate effective stress and limiting shear strength. Figure B-12b compares the Fourier spectra for elastic and plastic soil profiles against the input bedrock spectrum using a cut-off frequency of 20 Hz. It is evident from the figure that there is an amplification of the Fourier amplitudes for the free-field response compared with the bedrock. There is a notable increase in amplitude for the plastic soil model over the elastic soil model, suggesting that the reduction in soil stiffness reduces the natural frequency of the homogeneous layer. The increase in acceleration and amplitude may be attributed to the fact that the first natural frequency of the elastic homogenous layer is

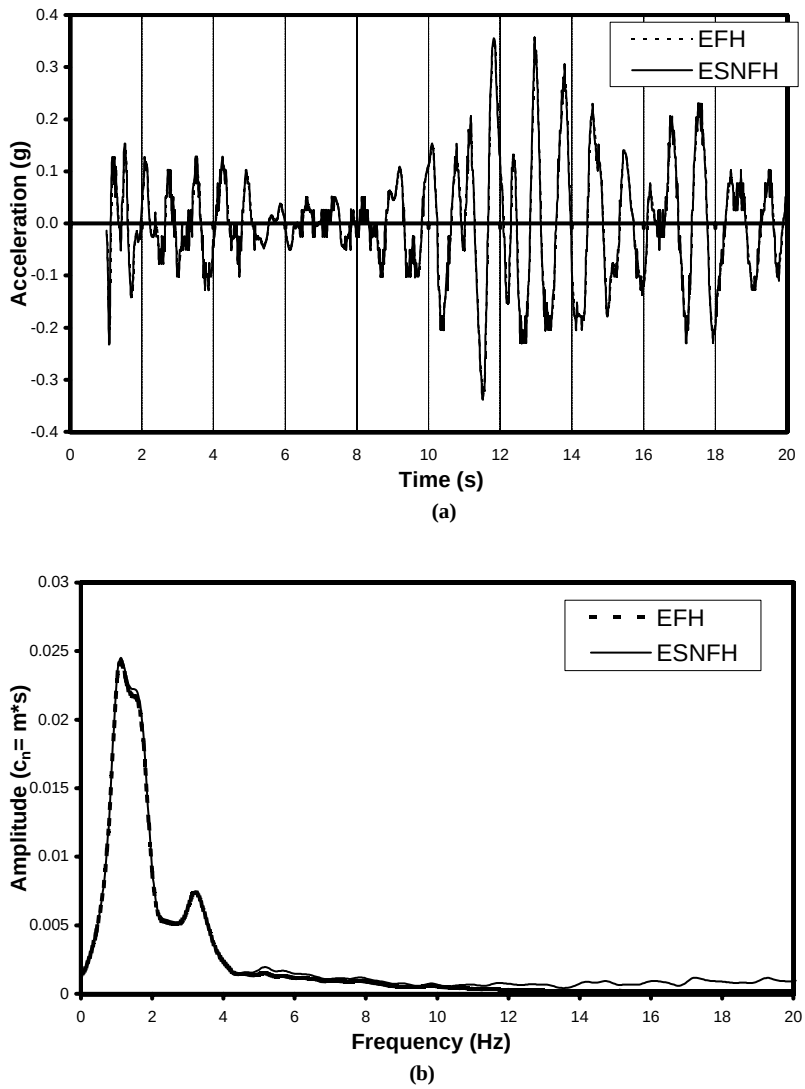

Figure B-13. The corresponding acceleration and Fourier spectrum for ESNFH compared with EFH. (a) Comparison between calculated accelerations for elastic free-field (EFH) and floating pile head (ESNFH) for a homogeneous elastic soil profile. (b) Fourier spectrum for the response of the elastic soil free-field and floating pile head.

slightly greater than 2 Hz, whereas the natural frequency of the plastic soil layer is slightly decreased and became closer to the predominant frequency at the free-field (approximately 1.5 Hz). For higher frequencies (see Figure B-11b), the small amplitude peaks seen at the bedrock level diminish as the seismic waves propagate throughout the soil until they reach the free-field. Both the elastic and plastic free-field amplitudes diminish at frequencies higher than 10 Hz, above which little response is induced in most structures.

Similar results for the floating and socketed pile-head response are plotted in Figures B-13 and B-14. Figures B-13a and B-13b represent the corresponding acceleration and Fourier spectrum for ESNFH compared with EFH. The diagrams are almost identical, except the Fourier amplitudes are slightly greater for the floating pile (especially for a frequency above 5 Hz). Figure B-14 shows the response of the ESNSH socketed pile case. Again, the overall acceleration of the pile head is similar to that of the elastic free-field. The Fourier amplitudes of the socketed pile (no separation) show both a decrease and an increase in magnitude over the elastic free-field, depending on the frequency range. At the predominant frequency amplitude (2 Hz), ESNSH seems to slightly decrease compared with EFH, and at frequencies above and below the predominant frequency, the amplitudes are increased. The increased stiffness of the system caused by the socketed pile may be responsible for the increased amplitude at higher frequency ranges compared with that of the free-field.

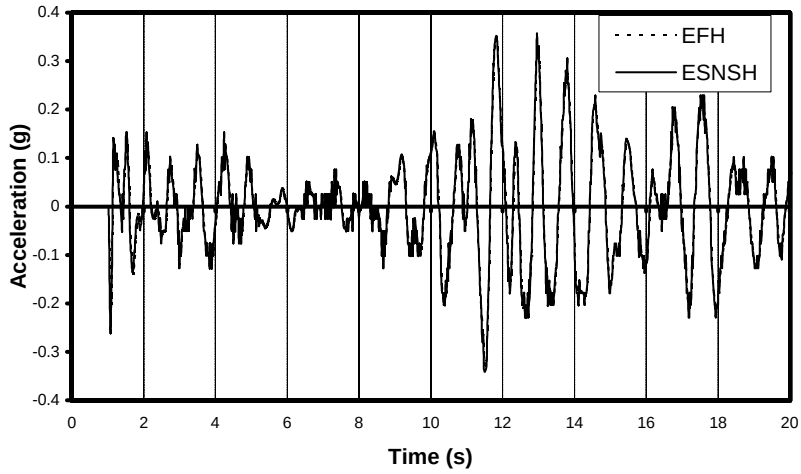

(a)

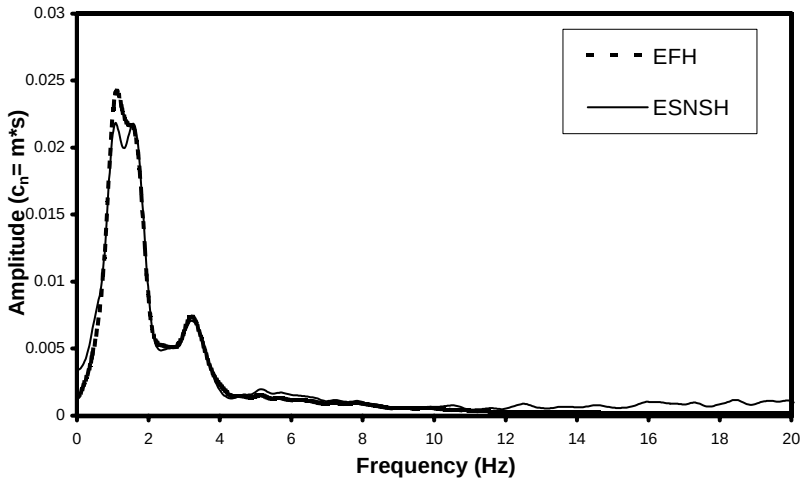

(b)

Figure B-14. Response of the ESNSH socketed pile case. (a) Comparison between calculated accelerations for elastic free-field (EFH) and socketed pile (ESNSH) for a homogeneous soil profile. (b) Fourier spectrum for the response at the plastic soil free-field and socketed pile head.

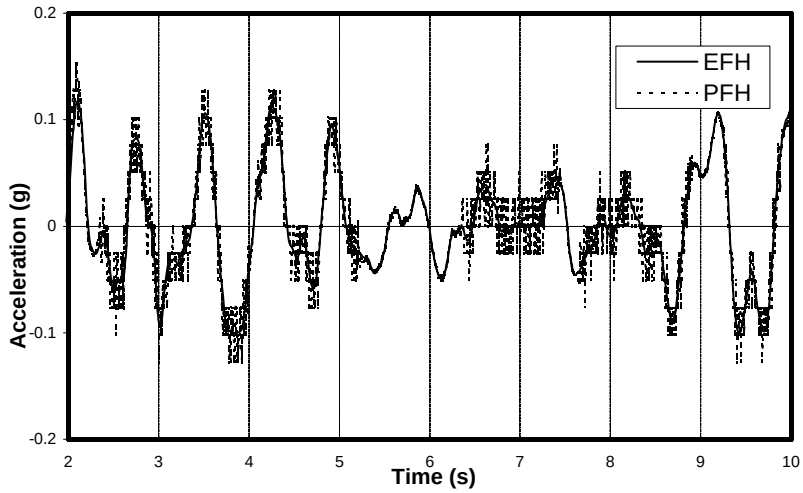

Figure B-15. EFH and PFH response (elastic and plastic free-field, E_s = 20 000 kPa).

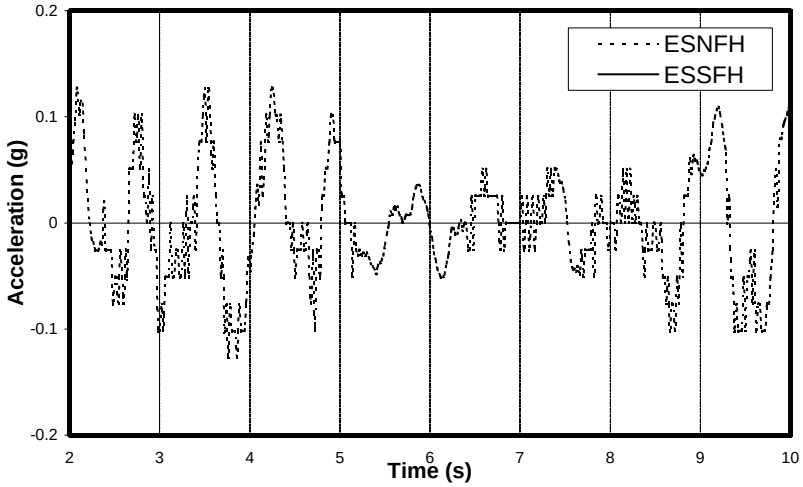

Figure B-16. Pile-head response for floating pile (elastic, elastic with gapping).

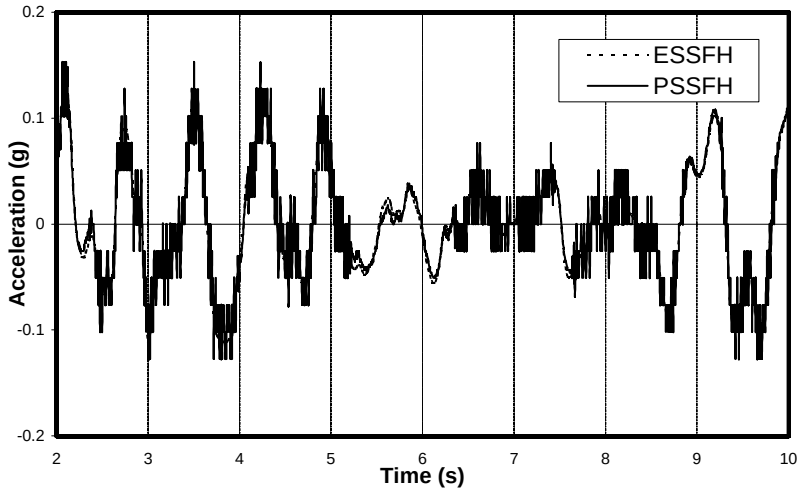

Figure B-17. Pile-head response for floating pile (elastic gapping, plastic gapping).

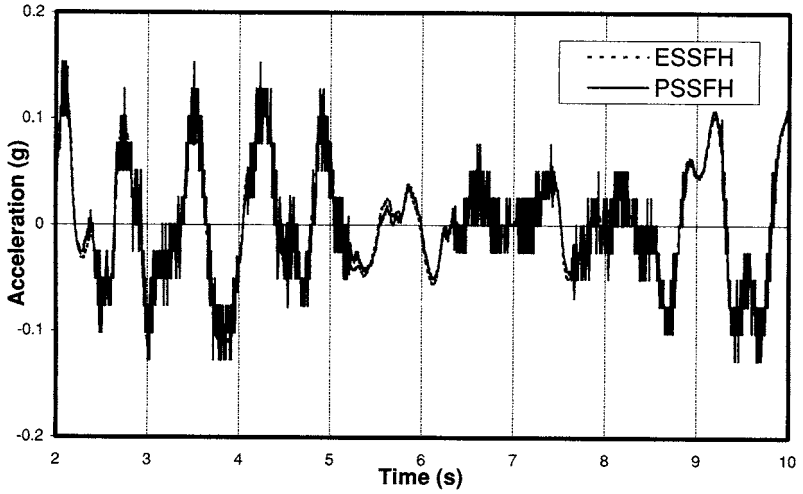

Figure B-18. Pile-head response for floating and socketed pile (plastic gapping).

Figure B-16 introduces the effects of separation between the pile and soil for the floating pile case. Only the 2- through 10-s interval is shown to provide a more detailed analysis. The overall response is very similar for both cases shown in Figure B-16. The floating pile with gapping seems to eliminate small fluctuations of acceleration seen when no gapping was allowed.

Figure B-17 introduces the effects of the soil plasticity in addition to separation for the floating pile. PSSFH is compared with the elastic model (ESSFH), and the results are very similar. The random scatter shown by introducing plasticity may be attributed to the solution procedure used in the finite element program. For convergence reasons, smaller time steps had to be used for the plastic soil model, which led to numerical instabilities. Figure B-18 compares the floating and socketed pile-head response including both separation and soil nonlinearity. The floating pile showed slightly higher peaks over the socketed pile, but the response remained almost identical.

Kinematic Interaction in Pile Groups

Modeling the kinematic response of pile groups, accounting rigorously for all the factors that influence the response, is a formidable task; therefore, most of the investigations on the seismic soil-pile interactions use linear analyses or simple idealized systems.

Analyses of the kinematic response of a single pile and of pile groups have been reported by Takemiya and Yamada (*11*), Flores-Berrones and Whitman (*12*), Gazetas (*13*) and Tazoh et al. (*14*). These studies, however, had very limited parametric results. Ahmad and Mamoon (*15*) and Fan et al. (*16*) attempted to fill this gap by providing comprehensive parametric studies for the kinematic response of piles. The results of these two studies are summarized herein.

Ahmad and Mamoon (*15*) examined the response of single piles under vertically and obliquely incident SH, SV, and P harmonic waves using a hybrid boundary element formulation. The piles were modeled using compressible beam-column elements, and the soil was modeled as a hysteretic viscoelastic half-space. They found that the pile-soil stiffness ratio, angle of incidence, and excitation frequency have significant influence on the seismic responses of piles. The results from the limited cases considered in their study suggested that in the low-frequency range, piles essentially follow the ground motion. This conclusion is similar to what was observed from the analyses presented earlier in this appendix. Ahmad and Mamoon also found that at higher frequencies, piles seem to remain relatively still while the free-field soil mass moves considerably. This filtering effect was found to be severe for a vertically incident wave, gradually diminishing for a more obliquely incident one. Furthermore, they found that flexible piles undergo significant bending under seismic excitation whereas rigid piles tend to show almost low, uniform rigid body motion. Obliquely incident waves produce higher displacement than did a vertically incident one throughout the pile depth. In the low-frequency range, vertically incident waves produce higher rotations of the pile head, but in the higher-frequency range, the opposite trend was observed.

Fan et al. (*16*) performed an extensive parametric study using the boundary element solution proposed by Kaynia and Kausel (*17*) to develop dimensionless graphs for pile-head deflections versus the free-field response for various soil profiles subjected to vertically propagating harmonic waves. Fan et al. (*16*) also used the approach developed by Makris and Gazetas (*18*), in which free-field accelerations are applied to a one-dimensional Beam-on-Dynamic-Winkler-Foundation model with frequency-dependent springs and dashpots to analyze the response of floating single piles and pile groups. Both approaches are essentially linear (or equivalent linear) analyses.

Makris and Gazetas (*18*) studied the kinematic response of single piles, one-row pile groups, and square groups of piles. They considered soil profiles with constant soil modulus, linearly increasing soil modulus with depth, and two distinct constant values above and below a depth $z = L/2$. Each pile-foundation-soil system was excited by vertically propagating harmonic shear free-field waves.

The results of the analyses were portrayed in the form of kinematic displacement factors (plotted versus dimensionless frequency, a_0) defined as the response of the pile cap normalized by the free-field motion. The investigated parameters were the ratio of the effective pile modulus to the soil modulus, the piles spacing-to-diameter ratio, and the pile's slenderness ratio. Inspection of the results revealed the following trends:

1. The general shape of the kinematic displacement factor, I_u, consists of three fairly distinct regions in the frequency range of greatest interest ($a_0 < 0.5$):
   - A low-frequency region ($0 < a_0 < 0.1$–0.3) in which $I_u \approx 1$, meaning the piles follow closely the deformations of the ground.
   - An intermediate-frequency region (0.1–$0.2 < a_0 < 0.3$–0.4) characterized by I_u declining rapidly with frequency, which showed increasing incompatibility between the movement of a pile and the surrounding soil.
   - A relatively high-frequency region ($a_0 > 0.3$–0.4) in which I_u fluctuates around an essentially constant value of about 0.2–0.4.
2. For the low- and intermediate-frequency regions, pile-soil-pile interaction effects on kinematic loading are not significant, but they are significant for pile-head loading (inertial interaction).

Summary and Conclusions—Kinematic Action

A three-dimensional finite element analysis was performed to investigate site effects and pile kinematic interaction effects

from seismic loading for a single pile. The analysis considered floating and socketed piles, including nonlinear soil properties, slippage and gapping at the pile-soil interface, and dissipation of energy through damping. Based on the results from the kinematic interaction study, it was concluded that the pile-head response (floating and socketed) closely resembled the free-field response for the low predominant frequency seismic loading. Fan et al. (*16*) reached a similar conclusion from their parametric study using a boundary element solution.

The following specific conclusions can be drawn:

- The effect of allowing a three-dimensional behavior as opposed to a one-dimensional behavior, with seismic loading applied in one dimension, was to decrease the acceleration amplitudes by a factor of 1.6 for the soil profiles considered.
- The effect of soil plasticity was to increase the Fourier amplitudes at the predominant frequency, but to slightly decrease the maximum acceleration amplitudes.
- The elastic kinematic interaction of single piles (both floating and socketed) has slightly amplified the bedrock motion when compared with the free-field response and has slightly decreased the Fourier amplitudes of all frequencies considered (0 through 20 Hz).
- Overall, the kinematic interaction response, including soil plasticity, slippage and gapping at the pile-soil interface, and damping, is equivalent to the free-field response. The conclusions, however, are limited to the pile and soil parameters and to the earthquake loading used in the analysis.
- For the frequency range of interest, pile-soil-pile interaction effects on kinematic loading are not significant, but are significant for pile-head loading (inertial interaction).

INERTIAL LOADING AND DYNAMIC *p-y* CURVES

Introduction

Most building and bridge codes use factored static loads to account for the dynamic effects of pile foundations. Although very low-frequency vibrations may be accurately modeled using factored loads, the introduction of nonlinearity, damping, and pile-soil interaction during transient loading may significantly alter the response. The typical frequency range of interest for earthquake loading is 0 to 10 Hz; therefore, the emphasis in the current study is on that range.

Novak et al. (*19*) developed a frequency-dependent pile-soil interaction model; however, the model assumes strictly linear or equivalent linear soil properties. Gazetas and Dobry (*20*) introduced a simplified linear method to predict fixed-head pile response accounting for both material and radiation damping and using available static stiffness (derived from finite element or any other accepted method). This method is not suitable for the seismic response analysis because of the linearity assumptions. In general, there is much controversy over advanced linear solutions (frequency domain), as they do not account for permanent deformation or gapping at the pile-soil interface.

Nogami et al. (*21*) developed a time domain analysis method for single piles and pile groups by integrating plane strain solutions with a nonlinear zone around each pile using *p-y* curves. El Naggar and Novak (*22, 23*) also developed a computationally efficient model for evaluating the lateral response of piles and pile groups based on the Winkler hypothesis, accounting for nonlinearity using a hyperbolic stress-strain relationship and slippage and gapping at the pile-soil interface. The model also accounts for the propagation of waves away from the pile and energy dissipation through both material and geometric damping.

The *p-y* curve (unit load transfer curve) approach is a widely accepted method for predicting pile response under static loads because of its simplicity and practical accuracy. In the present study, the model proposed by El Naggar and Novak (*23*) was modified to use existing or developed cyclic or static *p-y* curves to represent the nonlinear behavior of the soil adjacent to the pile. The model uses unit load transfer curves in the time domain to model nonlinearity and incorporates both material and radiation damping to generate dynamic *p-y* curves.

Model Description

Pile Model

The pile is assumed to be vertical and flexible with a circular cross section. Noncylindrical piles are represented by cylindrical piles with equivalent radius to accommodate any pier-pile configurations. The pile and the surrounding soil are subdivided into *n* segments, with pile nodes corresponding to soil nodes at the same elevation. The standard bending stiffness matrix of beam elements models the structural stiffness matrix for each pile element. The pile global stiffness matrix is then assembled from the element stiffness matrixes and is condensed to give horizontal translations at each layer and the rotational degree of freedom at the pile head.

Soil Model: Hyperbolic Stress-Strain Relationship

The soil is divided into *n* layers with different soil properties assigned to each layer according to the soil profile considered. Within each layer, the soil medium is divided into two annular regions as shown in Figure B-19. The first region is an inner zone adjacent to the pile that accounts for the soil nonlinearity. The second region is the outer zone that allows for wave propagation away from the pile and provides for the radiation damping in the soil medium. The soil reactions and the pile-soil interface conditions are modeled separately on both sides of the pile to account for slippage, gapping, and state of stress as the load direction changes.

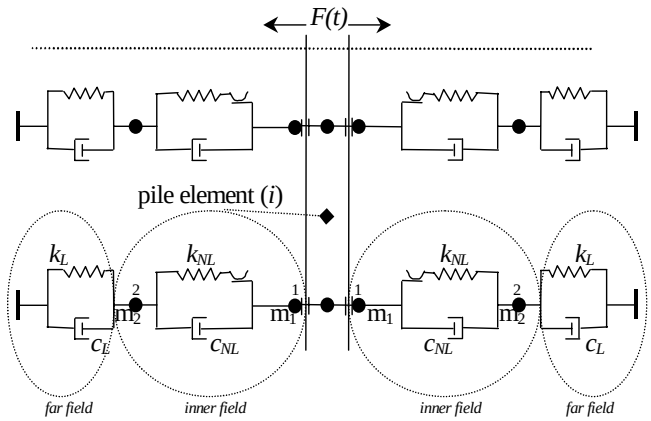

Figure B-19. Element representation of proposed model.

Inner Field Element. The inner field is modeled with a nonlinear spring to represent the stiffness and a dashpot to simulate material (hysteretic) damping. The stiffness is calculated assuming plane strain conditions. The inner field is a homogeneous isotropic viscoelastic, massless medium. The pile is rigid and circular. There is no separation at the soil-pile interface. Displacements are small. Novak and Sheta (*24*) obtained the stiffness (k_{NL}) under these conditions as

$$k_{NL} = \frac{8\pi G_m(1-\nu)(3-4\nu)\left[(r_0/r_1)^2+1\right]}{(r_0/r_1)^2+(3-4\nu)^2\left[(r_0/r_1)^2+1\right]\ln(r_1/r_0)-1}, \qquad \text{(B-5)}$$

where r_0 is the pile radius, r_1 is the outer radius of the inner zone, and ν is the Poisson's ratio of the soil stratum. The ratio r_1/r_0 depends on the extent of nonlinearity, which depends on the level of loading and on the pile's size. A parametric study showed that r_1/r_0 of 1.1 to 2 yielded good agreement between the stiffness of the composite medium (inner zone and outer zone) and the stiffness of a homogeneous medium (no inner zone) under small strain (linear) conditions. G_m is the modified shear modulus of the soil and is approximated, according to the strain level, by a hyperbolic law as

$$G_m = G_{\max}\left(\frac{1-\eta}{1+\eta}\right). \qquad \text{(B-6)}$$

$G_{\max}$ is the maximum shear modulus (small strain modulus) of the soil according to laboratory or field tests; η is a parameter = P/P_u (see Equation B-8). In the absence of actual measurements, maximum shear modulus for any soil layer can be calculated in this model by using the equation of Hardin and Black (*25*):

$$G_{\max} = \frac{3230(2.97-e)^2}{1+e}\,\sigma_0^{0.5} \qquad \text{kN/m}^2, \qquad \text{(B-7)}$$

where e is the void ratio, and σ_0 (kN/m^2) is the mean principal effective stress in the soil layer.

The parameter $\eta = P/P_u$ is the ratio of the horizontal soil reaction in the soil spring, P, to the ultimate resistance of the soil element, P_u. The ultimate resistance of the soil element is calculated using standard relations given by API (*4*). For clay, the ultimate resistance is given as a force per unit length of pile by

$$P_u = 3c_u d + \gamma x d + Jc_u x \qquad \text{or} \qquad \text{(B-8)}$$

$$P_u = 9c_u d\,, \qquad \text{(B-9)}$$

where

P_u = the minimum of the resistances calculated by Equations B-8 and B-9,
c_u = the undrained shear strength,
d = the diameter of the pile,
γ = the effective unit weight of the soil, and
J = an empirical coefficient dependent on the shear strength.

A value of $J = 0.5$ was used for soft clays (*26*) and $J = 1.5$ for stiff clays (*27*).

The corresponding criteria for the ultimate lateral resistance of sands at shallow depths P_{u1} or at large depths P_{u2} are as follows (*4*):

$$P_{u1} = A\left\{\gamma X\left[\frac{K_0 X\tan\phi\sin\beta}{\tan(\beta-\phi)\cos\alpha} + \frac{\tan\beta}{\tan(\beta-\phi)}(d + X\tan\beta\tan\alpha)\right]\right\} + A\gamma X\left\{K_0 X\tan\beta(\tan\phi\sin\beta-\tan\alpha) - K_a d\right\} \qquad \text{(B-10)}$$

$$P_{u2} = A\gamma X d\left[K_a\left(\tan^8\beta - 1\right) + K_0\tan\phi\tan^4\beta\right], \qquad \text{(B-11)}$$

where

A = an empirical adjustment factor dependent on the depth from the soil surface,
K_0 = the earth pressure coefficient at rest,
ϕ = the effective friction angle of the sand,
$\beta = \phi/2 + 45°$,
$\alpha = \phi/2$, and
K_a = the Rankine minimum active earth pressure coefficient defined as $K_a = \tan^2(45° - \phi/2)$.

In the derivation of Equation B-5, the inner field was assumed to be massless (*24*); therefore, the mass of the inner field is lumped equally at two nodes on each side of the pile: Node 1 adjacent to the pile and Node 2 adjacent to the outer field, as shown in Figure B-19.

Far-Field Element. The outer (i.e., far) field is modeled with a linear spring in parallel with a dashpot to represent the linear stiffness and damping (mainly radiation damping). The outer zone allows for the propagation of waves to infin-

ity. The complex stiffness, K, of a unit length of a cylinder embedded in a linear viscoelastic soil medium is given by Novak et al. (*19*):

$$K = G_{\max}[S_{u1}(a_0, \nu, D) + iS_{u2}(a_0, \nu, D)], \quad \text{(B-12)}$$

where $a_0 = \omega r_1/V_s$ is the dimensionless frequency: ω is the frequency of loading, V_s is the shear wave velocity of the soil layer, and D is the material damping constant of the soil layer. Figure B-20 shows the general variations of S_{u1} and S_{u2} with Poisson's ratio and material damping. Rewriting Equation B-12, the complex stiffness, K, can be represented by a spring coefficient, k_L, and a damping coefficient, c_L, as

$$K = k_L + ia_0c_L. \quad \text{(B-13)}$$

It can be noted from Figure B-20 that for the dimensionless frequency range between 0.05 and 1.5, S_{u1} maintains a constant value, and S_{u2} increases linearly with a_0. The predominant frequency of destructive earthquake loading falls within this range; therefore, for the purpose of a time domain analysis, the spring and dashpot constants, S_{u1} and S_{u2}, respectively, can be considered frequency independent and to depend only on Poisson's ratio. They are given as

$$k_L = G_{\max}S_{u1}(\nu) \quad \text{and} \quad \text{(B-14)}$$

$$c_L = \frac{2G_{\max}r_1}{V_s} S_{u2}(a_0 = 0.5, \nu). \quad \text{(B-15)}$$

Soil-Pile Interface

The soil-pile interface is modeled separately on each side of the pile, thus allowing gapping and slippage to occur independently on each side. The soil and pile nodes in each layer are connected using a no-tension spring. That is, the pile and soil will remain connected and will have equal displacement for compressive stresses. The spring is disconnected if tensile stress is detected in the soil spring to allow a gap to develop. This separation or gapping results in permanent displacement of the soil node that is dependent on the magnitude of the load. The development of such gaps is often observed in experiments, during offshore loading, and after earthquake excitation in clays. These gaps eventually fill in again over time until the next episode of lateral dynamic loading. The pile-soil interface for sands does not allow for gap formation, but instead the sand caves in, resulting in the virtual back-filling of sand particles around the pile during repeated dynamic loading. When the pile is unloaded, the sand on the tension side of the pile follows the pile with zero stiffness instead of remaining permanently displaced as in the clay model. In the unloading phase, the stiffness of the inner field spring is assumed to be linear in both the clay and sand models.

Group Effect

Because each pile in a group is affected not only by its own load, but also by the load and deflection of other piles in the group, the response of a pile group is greatly affected by the interaction between piles. For piles subjected to earthquake loading, this effect is important when considering the inertial loading, as has been pointed out by Fan et al. (*16*). For this reason, the group effect was also investigated in this study. As large displacements, pile-soil separation, and soil nonlinearity are expected to occur during earthquake events, the model developed by El Naggar and Novak (*23*), which is capable of these factors, was used in this study.

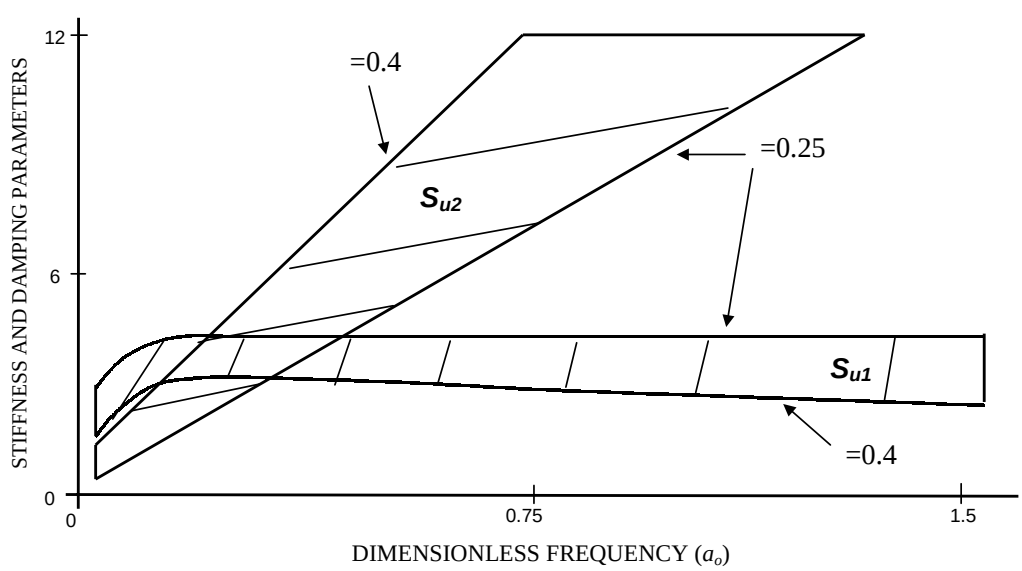

Figure B-20. Envelope of variations of horizontal stiffness and damping stiffness parameters for ν = 0.25–0.40 (after Novak et al. [19]).

Soil Model: p-y *Curve Approach*

The soil reaction to transient loading consists of stiffness and damping. The stiffness is established using the *p-y* curve approach, and the damping is established from analytical solutions that account for wave propagation. A similar approach was suggested by Nogami et al. (*21*) using *p-y* curves.

Based on physical tests, *p-y* curves can be used to relate pile deflections to the corresponding soil reaction at any depth (element) below the ground surface. The *p-y* curve represents the total soil reaction to the pile motion (i.e., the inner and outer zones' reactions combined). The total stiffness, k_{py}, derived from the *p-y* curve is equivalent to the true stiffness (real part of the complex stiffness) of the soil medium. Thus, referring to the hyperbolic law model, the combined inner zone stiffness (k_{NL}) and outer zone stiffness (k_L) can be replaced by a unified equivalent stiffness zone (k_{py}) as shown in Figure B-21a. Hence, to ensure that the true stiffness is the same for the two soil models, the flexibility of the two models is equated, that is,

$$\frac{1}{k_{py}} = \frac{1}{k_L} + \frac{1}{k_{NL}} . \tag{B-16}$$

The stiffness of the nonlinear strength is then calculated as

$$k_{NL} = \frac{(k_{py})(k_L)}{(k_L - k_{py})} . \tag{B-17}$$

The constant of the linear elastic spring, k_L, is established from the plane strain solution (i.e., Equation B-14). The static soil stiffness, k_{py} represents the relationship between the static soil reaction, *p*, and the pile deflection, *y*, for a given *p-y* curve at a specific load level. The *p-y* curves are established using empirical equations (*26, 28, 29*) or curve fit to measured data using an accepted method such as the modified Ramberg–Osgood model (*30*). In the present study, internally generated static *p-y* curves are established based on commonly used empirical correlations for a range of soil types.

Damping

The damping (imaginary part of the complex stiffness) is incorporated into both the *p-y* approach and the hyperbolic model to allow for energy dissipation throughout the soil. The nonlinearity in the vicinity of the pile, however, drastically reduces the geometric damping in the inner field; therefore, both material and geometric (radiation) damping are modeled in the outer field. A dashpot is connected in parallel to the far-field spring, and its constant is derived from Equation B-15. If the material damping in the inner zone is to be considered, a parallel dashpot with a constant c_{NL} to be suitably chosen may be added as shown in Figure B-21b. The addition of the damping resistance to static resistance represented by the static unit load transfer (the *p-y* curve) tends to increase the total resistance as shown in Figure B-22.

Static p-y *Curve Generation for Clay*

The general procedure for computing *p-y* curves in clays both above and below the groundwater table and corresponding parameters are recommended by Matlock (*26*) and Bhushan et al. (*27*), respectively. The *p-y* relationship was based on the following equation:

$$\frac{p}{P_u} = 0.5\left(\frac{y}{y_{50}}\right)^n , \tag{B-18}$$

where

p = soil resistance,
y = deflection corresponding to p,
P_u = ultimate soil resistance from Equations B-8 and B-9,
n = a constant relating soil resistance to pier-pile deflection, and
y_{50} = corrected deflection at one-half the ultimate soil reaction determined from laboratory tests.

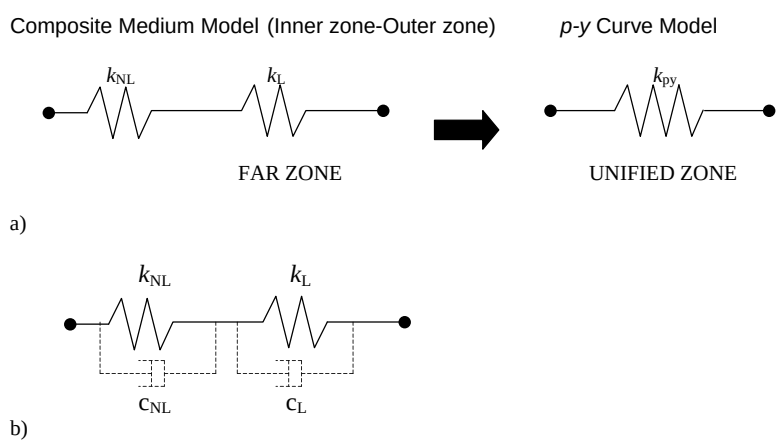

Figure B-21. Soil model: (a) composite medium and p-y *curve; (b) inclusion of damping.*

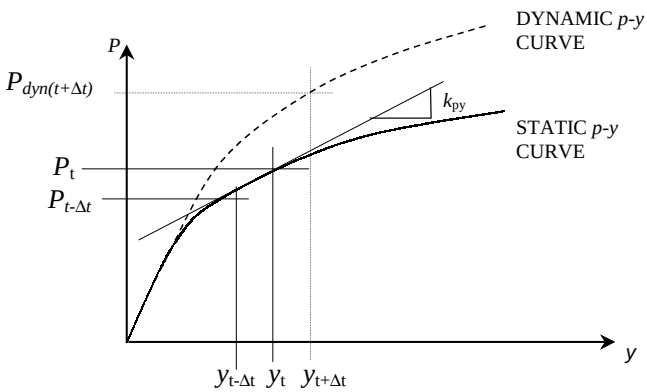

Figure B-22. Determination of stiffness (k_{py}) *from an internally generated static* p-y *curve to produce a dynamic* p-y *curve (including damping).*

The tangent stiffness constant, k_{py}, of any soil element at time step $t + \Delta t$ is given by the slope of the tangent to the *p-y* curve at the specific load level, as shown in Figure B-22. This slope is established from the soil deflections at time steps t and $t - \Delta t$ and from the corresponding soil reactions calculated from Equation B-18, that is,

$$k_{py(t+\Delta t)} = \frac{p_t - p_{t-\Delta t}}{y_t - y_{t-\Delta t}} . \qquad \text{(B-19)}$$

Therefore, Equations B-14 and B-19 can be substituted into Equation B-17 to obtain the nonlinear stiffness representing the inner field element in the analysis. Thus, the linear and nonlinear qualities of the unit load transfer curves have been logically incorporated into the outer and inner zones, respectively.

Static p-y *Curve Generation for Sand*

Several methods have been used to experimentally obtain *p-y* curves for sandy soils. Abendroth and Greimann (*31*) performed 11 scaled pile tests and used a modified Ramberg–Osgood model to approximate the nonlinear soil resistance and displacement behavior for loose and dense sand. The most commonly used criteria for development of *p-y* curves for sand were proposed by Reese et al. (*32*), but tend to give very conservative results. Bhushan et al. (*33*) and Bhushan and Askari (*34*) used a different procedure based on full-scale load test results to obtain nonlinear *p-y* curves for saturated and unsaturated sand. A step-by-step procedure for developing *p-y* curves in sands, based on Bhushan and Haley (*35*) and Bhushan et al. (*33*), was used to estimate the static unit load transfer curves for different sands below and above the water table. The procedure used to generate *p-y* curves for sand differs from that suggested for clays. The secant modulus approach is used to approximate soil reactions at specified lateral displacements. The soil resistance in the static *p-y* curve model can be calculated using the following equation:

$$p = (k)(x)(y)(F1)(F2) , \qquad \text{(B-20)}$$

where k is a constant that depends on the lateral deflection y (i.e. k decreases as y increases) and relates the secant modulus of soil for a given value of y to depth ($E_s = kx$), and x is the depth at which the *p-y* curve is being generated. $F1$ and $F2$ are density and groundwater (saturated or unsaturated) factors, respectively, and can be determined from Meyer and Reese (*36*). The main factors affecting k are the relative density of the sand (loose or dense) and the level of lateral displacement. The secant modulus decreases with increasing displacement, and, thus, the nonlinearity of the sand can be modeled accurately. This analysis assumes linear increase of the soil modulus with depth (but varies nonlinearly with displacement at each depth), which is typical for many sands.

Equation B-20 was used to establish the *p-y* curve at a given depth. The tangent stiffness k_{py} (needed in the time domain analysis), which represents the tangent to the *p-y* curve at the specific load level, was then calculated using Equation B-19, based on calculated soil reactions from the corresponding pile displacements for two consecutive time steps (using Equation B-20).

Degradation of Soil Stiffness

Transient loading, especially cyclic loading, may result in a buildup of pore water pressures, or a change of the soil structure, or both. Both pore pressures and structural changes can cause the shear strain amplitudes of the soil to increase with increasing number of cycles (*37*). Idriss et al. (*37*) reported that the shear stress amplitude decreased with increasing number of cycles for harmonically loaded clay and saturated sand specimens under strain-controlled undrained conditions. These studies suggest that repeated cyclic loading results in the degradation of the soil stiffness. For cohesive soils, the value of the shear modulus after N cycles, G_N, can be related to its value in the first cycle, G_{max}, by

$$G_N = \delta G_{max} , \qquad \text{(B-21)}$$

where the degradation index, δ, is given by $\delta = N^{-t}$, and t is the degradation parameter defined by Idriss et al. (*37*). This is incorporated into the proposed model by updating the nonlinear stiffness, k_{NL}, by an appropriate factor in each loading cycle.

Time Domain Analysis and Equations of Motion

The time domain analysis was used in order to include all aspects of nonlinearity and to examine the transient response logically and realistically. The governing equation of motion is given by

$$[M]\{\ddot{u}\} + [C]\{\dot{u}\} + [K]\{u\} = \{F(t)\}, \qquad \text{(B-22)}$$

where $[M]$, $[C]$, and $[K]$ are the global mass, damping, and stiffness matrixes, and $\{\ddot{u}\}$, $\{\dot{u}\}$, $\{u\}$, and $F(t)$ are acceleration, velocity, displacement, and external load vectors, respectively. In Figure B-19, the equations of motion at Node 1 (adjacent to the inner field) and Node 2 (adjacent to the outer field) are

$$m_1\ddot{u}_1 + c_{NL}(\dot{u}_1 - \dot{u}_2) + k_{NL}(u_1 - u_2) = F_1 \qquad \text{(B-23)}$$

$$m_2\ddot{u}_2 - c_{NL}(\dot{u}_1 - \dot{u}_2) - k_{NL}(u_1 - u_2) = F_2\,, \qquad \text{(B-24)}$$

where u_1 and u_2 are displacements of Nodes 1 and 2, F_1 is the force in the nonlinear spring including the confining pressure, and F_2 is the soil resistance at Node 2. The equation of motion for the outer field is written as

$$c\ddot{u}_2 + k_L u_2 = -F_2\,. \qquad \text{(B-25)}$$

Assuming compatibility and equilibrium at the interface between the inner and outer zones leads to the following equation, which is valid for both sides of the pile:

$$\begin{vmatrix} F_1 \\ 0 \end{vmatrix} = \begin{vmatrix} Am_1 + B(c_L + c_{NL}) + k_{NL} & -k_{NL} - Bc_{NL} \\ -k_{NL} - Bc_{NL} & k_{NL} + Am_2 + B(c_L + c_{NL}) + k_L \end{vmatrix} \begin{vmatrix} u_1 \\ u_2 \end{vmatrix} + \begin{vmatrix} F_1^{i-1} \\ F_2^{i-1} \end{vmatrix}, \qquad \text{(B-26)}$$

where F_1^{i-1} and F_2^{i-1} are the sums of inertia forces and soil reactions at Nodes 1 and 2, respectively. The values A and B are constants of numerical integration for inertia and damping, and m is mass.

The linear acceleration assumption was used, and the Newmark β method was implemented for direct time integration of the equations of motion. The modified Newton–Raphson iteration scheme was used to solve the nonlinear equilibrium equations.

Verification of the Analytical Model

Verification of Clay Model

Different soil profiles were considered in the analysis. Figure B-23 shows the typical pile-soil system and the soil profiles considered including linear and parabolic soil profiles. The *p-y* model was first verified against the hyperbolic model (*12*). Figures B-24 and B-25 compare the dynamic soil reaction and pile-head response for both the hyperbolic and *p-y* curve models for a single reinforced concrete pile in soft clay. A pile 0.5 m in diameter and 15 m long was used with an elastic modulus (E_p) equal to 35 GPa. A parabolic soil profile with the ratio E_p/E_s = 1,000 at the pile base was assumed. The undrained shear strength of the clay was assumed to be 25 kPa. Figure B-24 shows the calculated dynamic soil reactions for a prescribed harmonic displacement of an amplitude equal to 0.03d at a frequency of 2 Hz at the pile head. It can be noted from Figure B-24 that the soil reactions obtained from the two models are very similar and approach stability after five cycles. The pattern shown in Figure B-24 is also similar to that obtained by Nogami et al. (*21*), showing an increasing gap and stability after approximately five cycles. Figure B-25 shows the displacement-time history of the pile head installed in the same soil profile. The load was applied at the pile head and was equal to approximately 10 percent of the ultimate lateral loading capacity of the pile. The hyperbolic and *p-y* curve models show very similar responses at the pile head, and both stabilize after approximately five cycles.

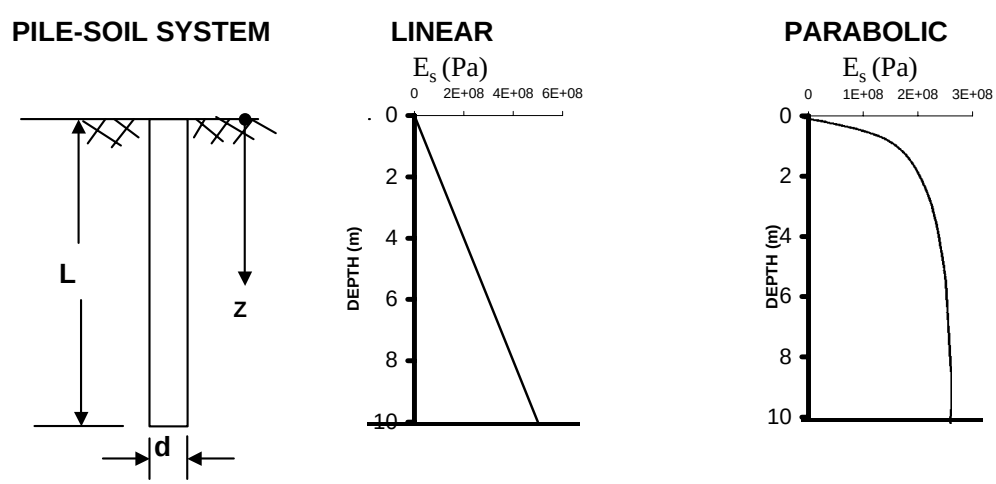

Figure B-23. Soil modulus variation for profiles considered in the analysis.

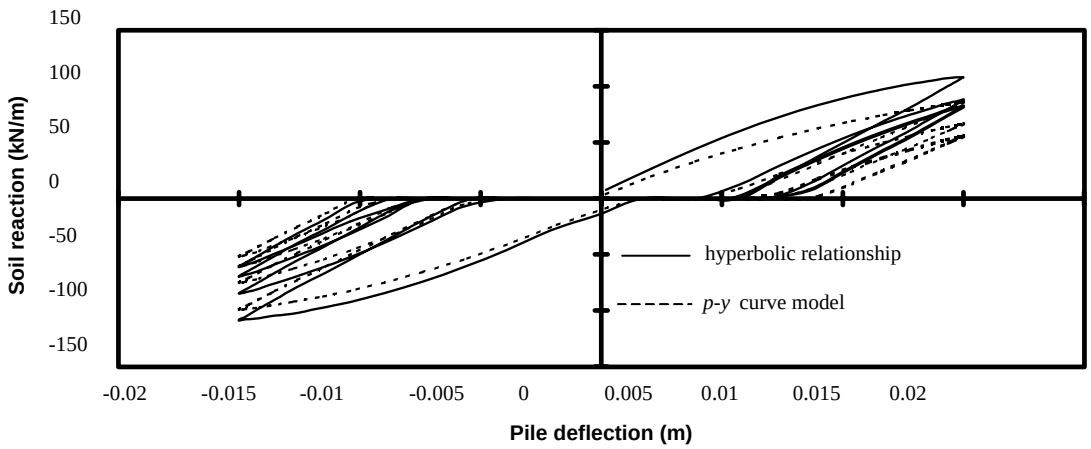

Figure B-24. Calculated dynamic soil reactions at 1.0-m depth (for a prescribed harmonic displacement at pile head with amplitude = 0.015 m, L/d *= 30).*

The dynamic soil reactions are, in general, larger than the static reactions because of the contribution from damping. Employing the same definition used for static *p-y* curves, dynamic *p-y* curves can be established to relate pile deflections to the corresponding dynamic soil reaction at any depth below the ground surface. The proposed dynamic *p-y* curves are frequency dependent. These dynamic *p-y* curves can be used in other static analyses that are based on the *p-y* curve approach to account approximately for the dynamic effects on the soil reactions to transient loading.

Figures B-26 and B-27 show dynamic *p-y* curves established at two different clay depths for a prescribed harmonic displacement at the pile head with an amplitude equal to 0.05 d, for a frequency range from 0 to 10 Hz. The shear modulus of the soil was assumed to increase parabolically along the pile length. A concrete pile 12.5 m in length and 0.5 m in diameter was considered in the analysis. The elastic modulus of the pile material was assumed to be 35 GPa and the ratio E_p/E_s = 1,000 (at the pile base). Both the *p-y* curve and hyperbolic models were used to analyze the pile response. The dynamic soil reaction (normalized by the ultimate pile capacity, P_{ult}) obtained from the *p-y* curve model compared well with that obtained from the hyperbolic relationship model, especially for lower frequencies, as can be noted from Figures B-26 and B-27. It can also be observed from Figures B-26 and B-27 that the soil reaction increased as the frequency increased. This increase was more evident in the results obtained from the *p-y* curve model.

Verification of Sand Model

The *p-y* curve and hyperbolic models were used to analyze the response of piles installed in sand. The sand was assumed to be unsaturated, and a linear soil modulus profile was adopted. The same pile as was used in the previous case was considered. Figure B-28 shows the calculated dynamic soil reactions at a 1-m depth for a prescribed harmonic dis-

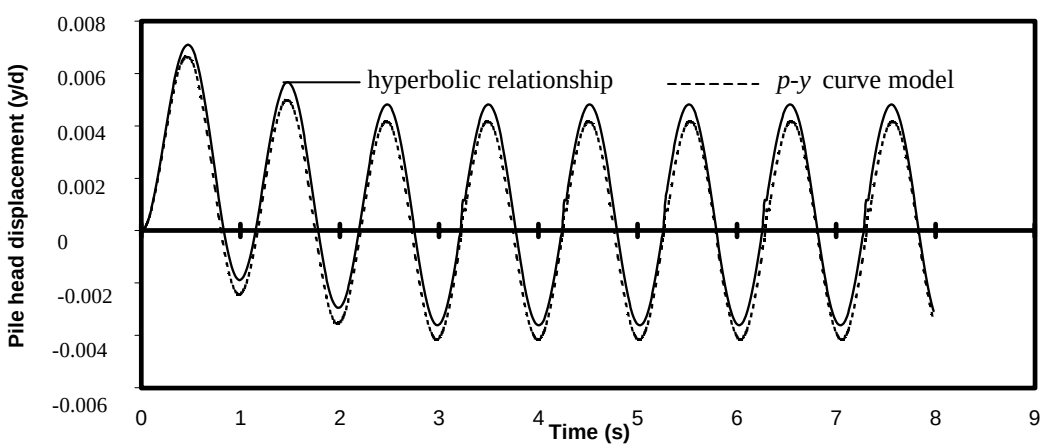

*Figure B-25. Pile-head response under applied harmonic load with amplitude equal to 10 percent of the ultimate load (*L/d *= 30,* E_p/E_s (L) *= 1000, linear profile).*

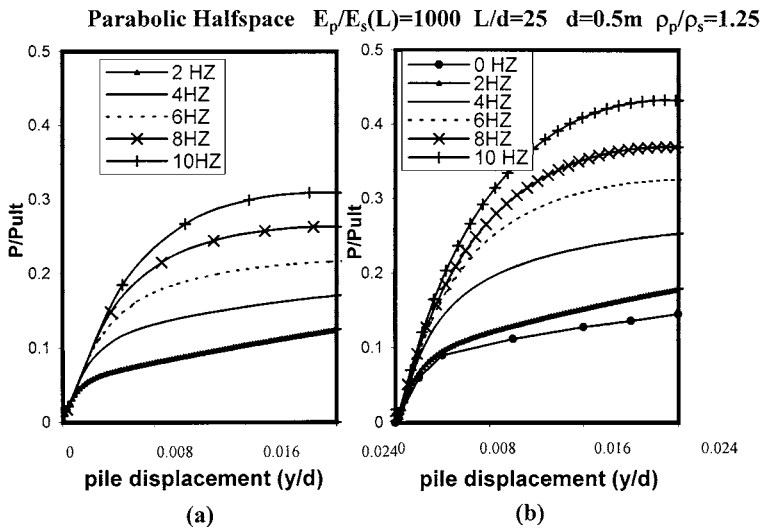

Figure B-26. Calculated dynamic p-y *curves at 1.5-m depth (for a prescribed harmonic displacement at pile head with amplitude equal to 0.05 d) using (a) hyperbolic model and (b)* p-y *curve model.*

placement with an amplitude equal to 0.0375 d at the pile head with a frequency of 2 Hz. As can be seen in Figure B-28, the two models feature very similar dynamic soil reactions. It should be noted that the soil reactions at both sides of the pile are traced independently. The upper part of the curve in Figure B-28 represents the reactions for the soil element adjacent to the right face of the pile when it is loaded rightward. The lower part represents the reactions of the soil element adjacent to the left face of the pile as it is loaded leftward. Both elements offer zero resistance to the pile movement when tensile stresses are detected in the nonlinear soil spring during unloading of the soil element on either side. The soil nodes, however, remain attached to the pile node at the same level, allowing the sand to "cave in" and fill the gap. Observations from field and laboratory pile testing have confirmed that, unlike clays, sands usually do not experience gapping during harmonic loading. Thus, both analyses realistically and logically model the physical behavior of the soil.

The pile-head displacement time histories obtained from the *p-y* curve and hyperbolic models for a pile installed in a sand with linearly varying elastic modulus caused by an applied harmonic load are shown in Figure B-29. It can be noted that good agreement exists between the results from the *p-y* curve model and hyperbolic model.

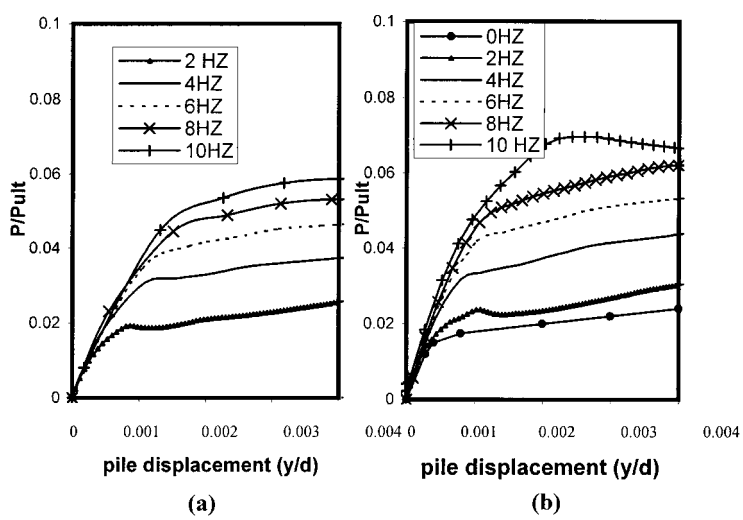

Figure B-27. Calculated dynamic p-y *curves at 3.0-m depth (for a prescribed harmonic displacement at pile head with amplitude equal to 0.05 d) using (a) hyperbolic model and (b)* p-y *curve model.*

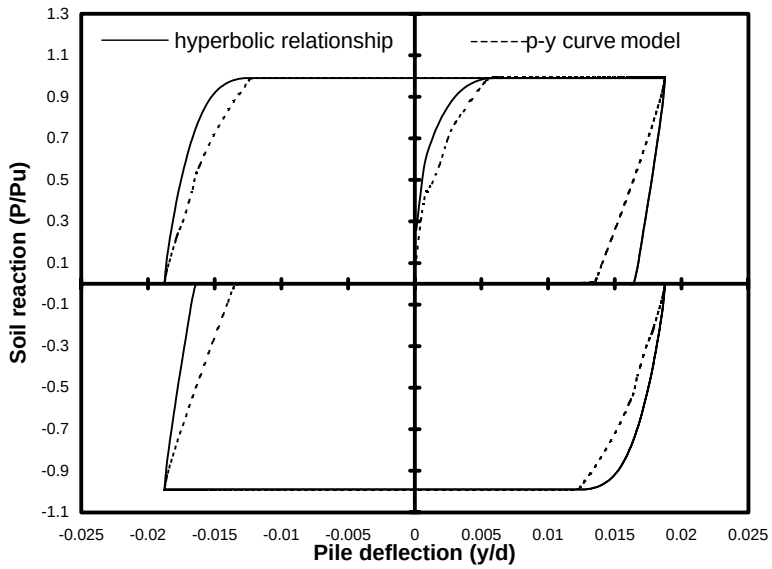

Figure B-28. Calculated dynamic soil reactions at 1.0-m depth (for a prescribed harmonic displacement at pile head with amplitude equal to 0.0375 d, L/d *= 25, and* E_p/E_s [L] *= 1000).*

Figures B-30 and B-31 show dynamic *p-y* curves established at two different depths for a prescribed harmonic displacement equal to 0.05 d at the pile head for a steel pile driven in sand for a frequency range from 0 to 10 Hz. The results from both the *p-y* curve and hyperbolic models displayed the same trend, as can be noted from Figures B-30 and B-31.

Validation of Dynamic Model with Lateral Statnamic Tests

In order to verify that the *p-y* curve model can accurately predict dynamic response, the model was employed to analyze a lateral Statnamic load test, and the computed response was compared with measured values.

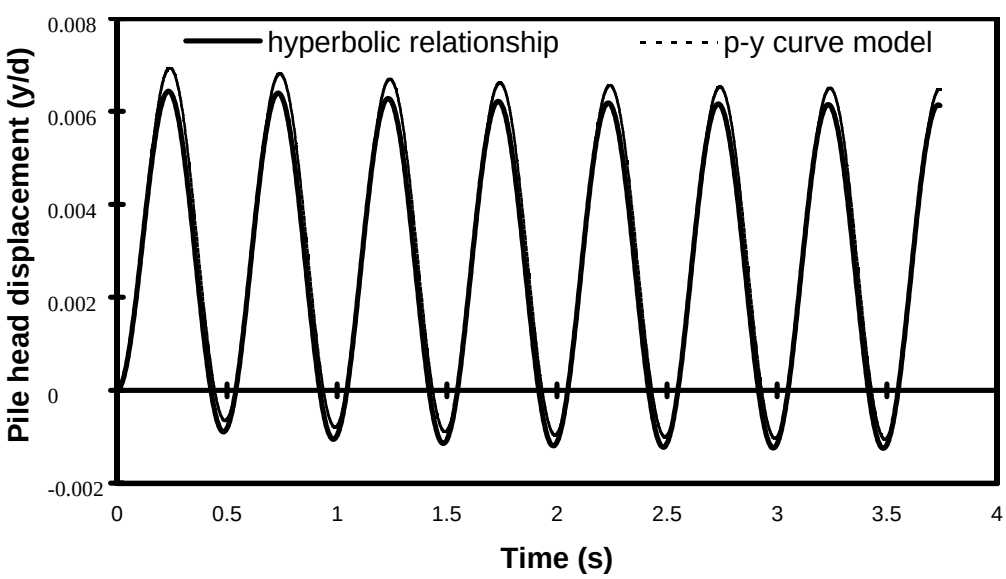

*Figure B-29. Pile-head response to applied harmonic load with an amplitude equal to 8 percent of the ultimate load (*L/d *= 25,* E_p/E_s (L) *= 1000, linear profile).*

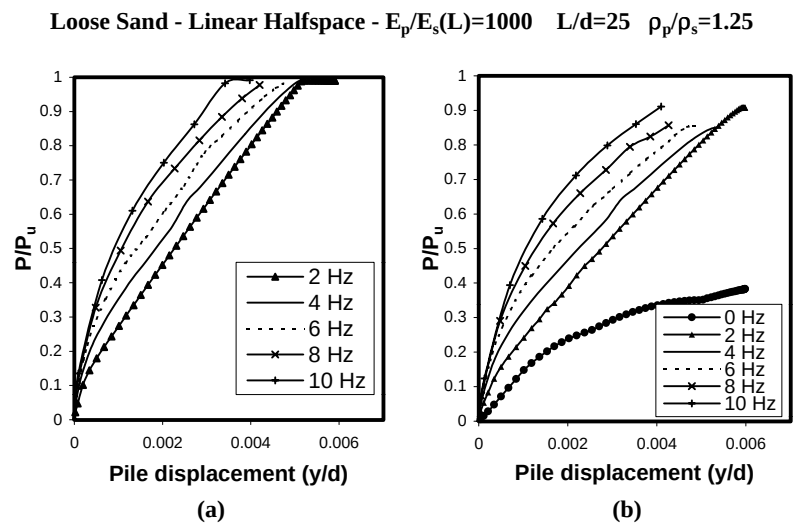

Figure B-30. Calculated dynamic p-y *curves at 3.0-m depth (for a prescribed harmonic displacement at pile head with amplitude equal to 0.05 d) using (a) hyperbolic model and (b)* p-y *curve model.*

The test site was located north of the New River at the Kiwi manoeuvres area of Camp Johnson in Jacksonville, North Carolina. The soil profile is shown in Figure B-32 and consists of medium-dense sand extending to the water table, underlain by a very weak, gray silty clay. There was a layer of gray sand at a depth of 7 m and a calcified sand stratum underlying that layer. The pile tested at this site was a cast-in-place reinforced concrete shaft with steel casing having an outer diameter of 0.61 m and a casing wall thickness of 13 mm. More details on the soil and pile properties and the loading procedure are presented by El Naggar (*38*). Statnamic testing was conducted on the pile 2 weeks after lateral static testing was performed. Statnamic loading tests were performed by M. James and P. Bermingham, both of Berminghammer Foundation Equipment, Hamilton, Ontario.

The computed lateral response of the pile head is compared with the measured response in Figure B-33 for two separate tests with peak load amplitudes of 350 kN and 470 kN. The agreement between the measured and computed values was excellent, especially for the first load test. The initial displace-

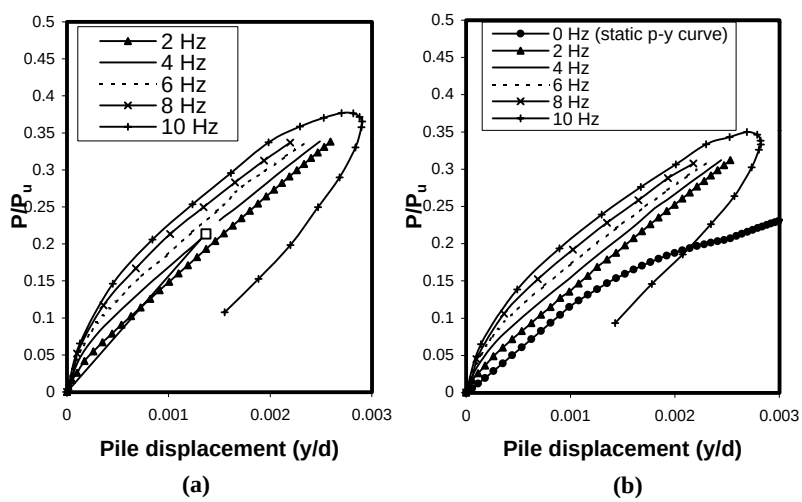

Figure B-31. Calculated dynamic p-y *curves at 4.0-m depth (for a prescribed harmonic displacement at pile head with amplitude equal to 0.05 d) using (a) hyperbolic model and (b)* p-y *curve model.*

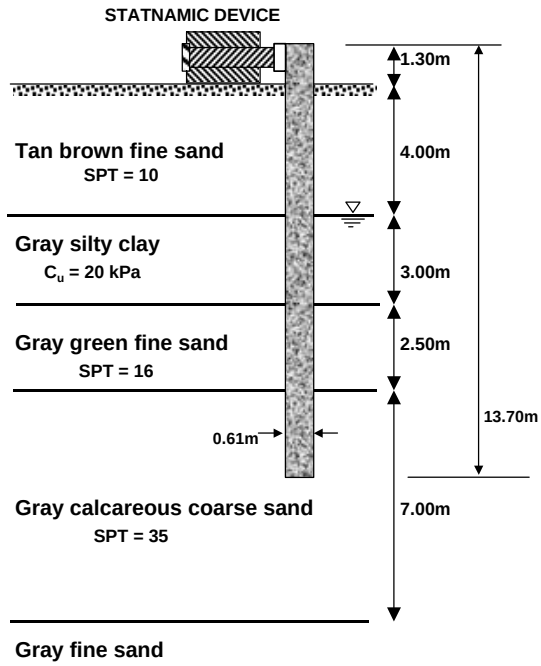

Figure B-32. Soil profile and Statnamic pile test set-up at Camp Johnson, Jacksonville.

ment was slightly adjusted for the computer-generated model to accommodate initial gapping that occurred because of the previous static test performed on the pile. The static *p-y* curve for the top soil layer was reduced significantly in order to model the loss of resistance caused by permanent gap developed near the surface.

Dynamic *p-y* Curve Generation

The dynamic *p-y* curves presented in Figures B-26 through B-28, B-30, and B-31 showed that a typical family of curves exists related to depth, much like the static *p-y* curve relationships. Thus, dynamic *p-y* curves could be established at any depth and be representative of the soil resistance at this specific depth. In this study, they were obtained at a depth equal to 1.5 mm, which was found to illustrate the characteristics of the dynamic *p-y* curves.

More dynamic *p-y* curves were generated using prescribed harmonic displacements applied at the pile head that allowed for the development of plastic deformation in the soil along the top quarter of the pile length. Steel pipe piles were considered in the analysis. It was assumed that sand had a linear soil profile and that the clay had a parabolic profile in order to match the soil profile employed to derive the static *p-y* curves used in the analysis. The soil shear wave velocity profiles and the pile properties are given in Figure B-34. The tests were divided into two separate cases involving clays (Case I) and sandy soils (Case II). Table B-1 summarizes the characteristics of each case and relevant pile and soil parameters. The dynamic *p-y* curves were generated over a frequency range of 0 to 10 Hz (2-Hz intervals) for different classifications of sand and clay based on standard laboratory and field measurements (standard penetration test–value, relative density, c_u, etc.). All results were obtained after one or two cycles of harmonic loading.

Results and Discussion

The results from the computational model showed a general trend of increasing soil resistance with an increase in the load frequency. The dynamic *p-y* curves obtained seem to have three distinct stages or regions. The initial stage (at small displacements) shows an increase in the soil resistance (compared with the static *p-y* curve) that corresponds to increasing the velocity of the pile to a maximum. This increase in the soil resistance is larger for higher frequencies. In the second stage, the dynamic *p-y* curves have almost the same slope as the static *p-y* curve for the same displacement. This stage occurs when velocity is fairly constant and, consequently, the damping contribution is also constant. The third stage of the dynamic *p-y* curve is characterized by a slope approaching zero as plastic deformations start to occur (similar to the static *p-y* curve at the same displacement). There is also a tendency for the dynamic curves to converge at higher resistance levels approaching the ultimate lateral resistance of the soil at depth *x*, P_u (determined from API research [*4*]).

The overall relationship between the dynamic soil resistance and loading frequency for each test was established in the form of a generic equation. The equation was developed from regression analysis relating the static *p-y* curve, frequency, and apparent velocity (ωy), so that

$$P_d = P_s\left[\alpha + \beta a_0^2 + \kappa a_0\left(\frac{\omega y}{d}\right)^n\right],\ P_d \le P_u \text{ at depth } x, \quad \text{(B-27)}$$

where

P_d = dynamic value of "*p*" on the *p-y* curve at depth *x* (N/m),
P_s = corresponding static soil reaction (obtained from the static *p-y* curve) at depth *x* (N/m),
a_0 = dimensionless frequency = $\omega r_0/V_s$,
ω = frequency of loading (rad/s),
d = pile diameter (m),
y = lateral pile deflection at depth *x* when soil and pile are in contact during loading (m), and
α, β, κ, and n = constants determined from curve fitting Equation B-27 to the computed dynamic *p-y* curves from all cases considered in this study.

A summary of the best-fit values for the constants is provided in Table B-2. The constant α is taken equal to unity to ensure that $P_d = P_s$, for $\omega = 0$. For large frequencies or displacements, the maximum dynamic soil resistance is limited to the ultimate static lateral resistance of the soil, P_u.

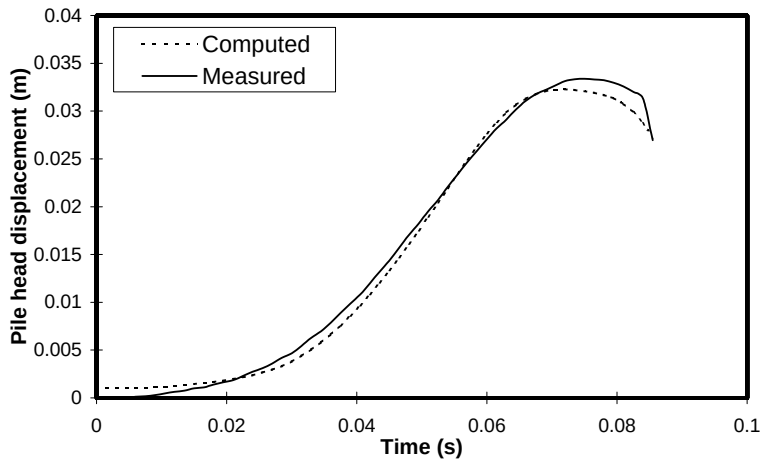

(a)

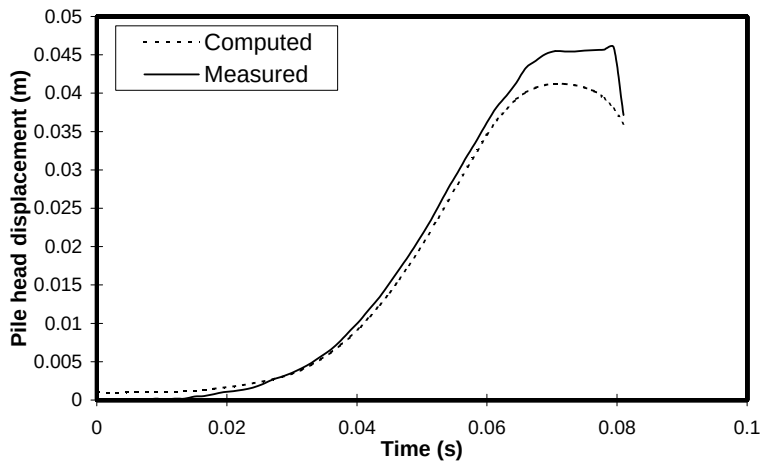

(b)

Figure B-33. Pile-head displacement for Statnamic test with peak load equal to (a) 350 kN and (b) 470 kN.

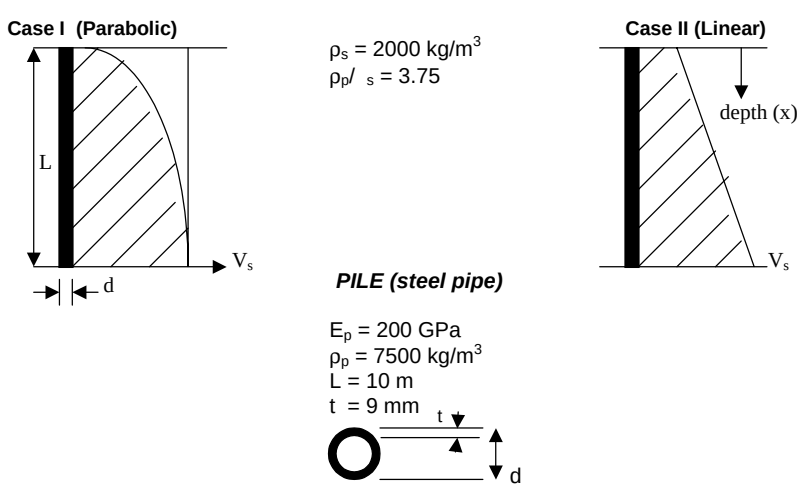

Figure B-34. Description of soil and pile properties for Case I and Case II.

TABLE B-1 Description of parameters used for each test case

CASE I (clays)	SOIL TYPE	C_u (kPa)	ν	*d* (m)	*L/d*	E_p/E_s	G_{max} (kPa)	V_s (m/s)
C1	SOFT CLAY	< 50	0.45	0.25	40	10000	6.6e6	70
C2	MEDIUM CLAY	80	0.45	0.25	40	4500	1.6e7	150
C3	STIFF CLAY	>100	0.45	0.25	40	1600	8.3e7	200

CASE II (sands)	SOIL TYPE	D_r (%)	ϕ	ν	*d* (m)	*L/d*	E_p/E_s	G_{max} (kPa)	V_s (m/s)
S4	LOOSE SAND (saturated)	35	32	0.3	0.25	40	6300	1.2e7	70
S5	MEDIUM SAND (saturated)	50	34	0.3	0.25	40	3800	2.0e7	100
S6	MEDIUM SAND (saturated)	50	34	0.3	0.50	20	3800	2.0e7	100
S8	DENSE SAND (saturated)	90	38	0.3	0.25	40	1580	4.7e7	150
S9	DENSE SAND (unsaturated)	90	38	0.3	0.25	40	790	9.7e7	220

NOTE: All values represent those calculated at a depth of 1.5 m.

TABLE B-2 Dynamic *p-y* curve parameter constants for a range of soil types*

SOIL TYPE	DESCRIPTION	α	β		κ	*n*
			$a_o < 0.025$	$a_o > 0.025$		
SOFT CLAY	$C_u < 50$ kPa $V_s < 125$ m/s	1	–180	–200	80	0.18
MEDIUM CLAY	$50 < C_u < 100$ kPa $125 < V_s < 175$ m/s	1	–120	–360	84	0.19
STIFF CLAY	$C_u > 100$ kPa $V_s > 175$ m/s	1	–2900	–828	100	0.19
MEDIUM-DENSE SAND (saturated)	$50 < D_r < 85$ % $125 < V_s < 175$ m/s	1	3320	1640	–100	0.1
MEDIUM-DENSE SAND (unsaturated)	$50 < D_r < 85$ % $125 < V_s < 175$ m/s	1	1960	960	–20	0.1
DENSE SAND (saturated)	$D_r > 85$ % $V_s > 175$ m/s	1	6000	1876	–100	0.15

* ($d = 0.25$, $L/d = 40$, $0.015 < a_o = \omega r_o/V_s < 0.225$); $P_d = P_s\left[\alpha + \beta a_o^{\,2} + \kappa a_o\left(\frac{\omega y}{d}\right)^n\right]$

Figures B-35 and B-36 show dynamic *p-y* curves established using Equation B-27 and the best-fit constants (as dashed lines). The approximate dynamic *p-y* curves established from Equation B-27 represented soft/medium clays and loose to medium-dense sands reasonably well. However, the accuracy is less for stiffer soils (higher V_s values). The precision of the fitted curves also increases with frequency ($\omega \geq 4$ Hz) where the dynamic effects are important. The low accuracy at a lower frequency ($a_0 < 0.02$) may be attributed to the application of the plane strain assumption in the dynamic analysis. This assumption is suitable for higher frequencies as the dynamic stiffness of the outer field model vanishes for $a_0 < 0.02$ because of the assumption of plane strain. Case C1 was also used to obtain dynamic *p-y* curves at depths of 1.0 m and 2.0 m to examine the validity of Equation B-27 to describe the dynamic soil reactions at other depths along the soil profile. The results showed that Equation B-27 (using the constants in Table B-2) predicted the dynamic soil reactions reasonably well.

Development of a Simplified Model

For many structural dynamics programs, soil-structure interaction is modeled using static *p-y* curves to represent the soil reactions along the pile length. However, the use of static *p-y* curves for dynamic analysis does not include the effects of velocity-dependent damping forces. The dynamic *p-y* curves established using Equation B-27 and the parameters given in Table B-2 allow for the generation of different dynamic *p-y* curves based on the frequency of loading and soil profile. Substituting dynamic *p-y* curves in place of traditional static *p-y* curves for analysis should result in better estimates of the response of structures to dynamic loading.

Alternatively, the dynamic soil reactions can be represented using a simple spring and dashpot model. This model can still capture the important characteristics of the nonlinear dynamic soil reactions. A simplified dynamic model that can be easily implemented into any general finite element program is proposed herein.

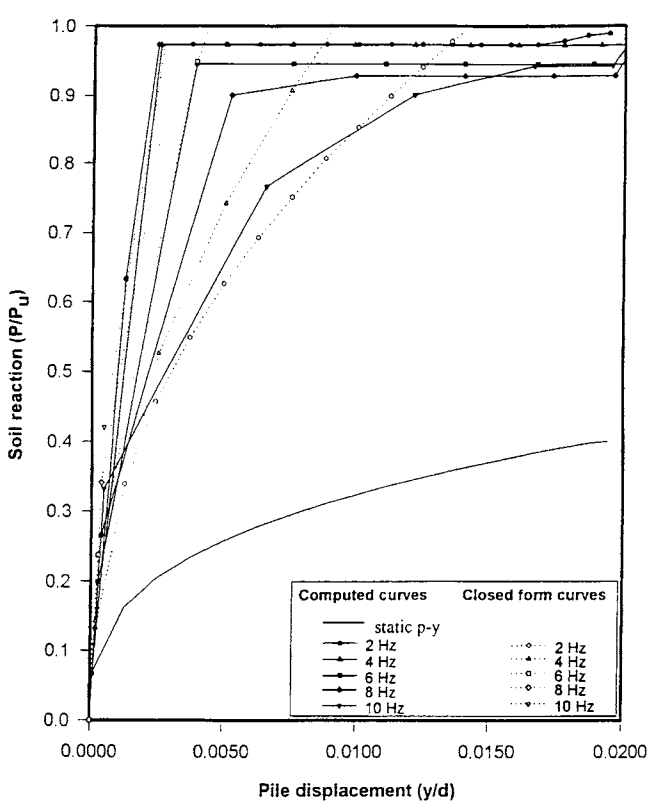

Figure B-35. Dynamic p-y *curves and static* p-y *curve for Case C1 (depth = 1.0 m).*

Complex Stiffness Model

As discussed previously, Equation B-27 can be used directly to represent the dynamic relationship between a soil reaction and a corresponding pile displacement. The total dynamic soil reaction at any depth is represented by a nonlinear spring whose stiffness is frequency dependent.

A more conventional and widely accepted method of calculating dynamic stiffness is through the development of the complex stiffness. The complex stiffness has a real part, K_1, and an imaginary part, K_2, that is,

$$P_d = Ky = (K_1 + iK_2)y \tag{B-28}$$

The real part, K_1 represents the true stiffness, *k;* the imaginary part of the complex stiffness, K_2, describes the out-of-phase component and represents the damping caused by the energy dissipation in the soil element. Because this damping component generally grows with frequency (resembling viscous damping), it can also be defined in terms of the constant of equivalent viscous damping (the dashpot constant) given by $c = K_2/\omega$. The dynamic *p-y* curve relation can be described as

$$P_d = (k + i\omega c)y = ky + c\dot{y}\,, \tag{B-29}$$

in which both *k* and *c* are real and represent the spring and dashpot constants, respectively, and $\dot{y} = dy/dt$ is velocity. Using Equation B-27, the dynamic *p-y* curve can be written in the form of Equation B-28, that is,

$$P_d = (K_1 + iK_2)y$$
$$= \left\{ \frac{P_s\alpha}{y} + i\,\frac{P_s\left(\beta a_0^2 + \kappa a_0\left(\frac{\omega y}{d}\right)^n\right)}{y} \right\} y. \tag{B-30}$$

The stiffness and damping constants are then calculated as

$$k = K_1 = \frac{P_s\alpha}{y} \quad \text{and} \tag{B-31}$$

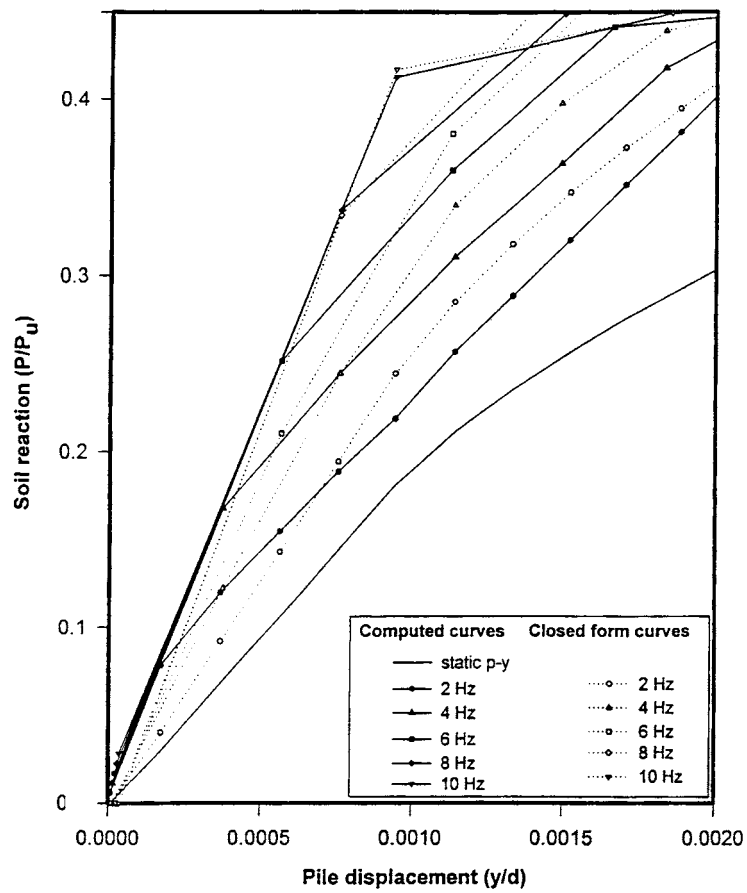

Figure B-36. Dynamic p-y *curves and static* p-y *curve for Case S5 (depth = 1.5 m).*

$$c = \frac{K_2}{\omega} = \frac{P_s\left(\beta a_0^2 + \kappa a_0\left(\frac{\omega y}{d}\right)^n\right)}{\omega y}. \qquad \text{(B-32)}$$

The complex stiffness can be generated at any depth along the pile using the static *p-y* curves and Equations B-31 and B-32.

Complex Stiffness Constants—Soft Clay Example

The complex stiffness constants were calculated for Test C1 (see Table B-2) using the method described in the previous section. The values of the true stiffness, *k*, were obtained for the range of displacements experienced by the pile for the frequency range from 0 to10 Hz. The stiffness parameter $(S_1)_{py}$ was defined as

$$(S_1)_{py} = \frac{k_{py}}{G_{\max}}. \qquad \text{(B-33)}$$

The constant of equivalent damping, *c*, was obtained by averaging the value from Equation B-32 for the range of velocities experienced by the pile for each frequency of loading. Then, the equivalent damping parameter $(S_2)_{py}$ was defined as

$$(S_2)_{py} = \frac{cV_s\omega}{G_{\max} r_0}. \qquad \text{(B-34)}$$

Figure B-37 shows the true stiffness calculated from the static *p-y* curve, and it can be noted that this stiffness is identical at all loading frequencies considered. There is a definite trend of decreasing stiffness with increased displacement because of the soil nonlinearity. The constant of equivalent damping presented in Figure B-38 shows a decreasing pattern with frequency that can be attributed to separation at the pile-soil interface. The values from Figures B-37 and B-38 can be directly input into a finite element program as spring and dashpot constants to obtain the approximate dynamic stiffness of a soil profile similar to Test C1.

Implementing Dynamic p-y *Curves in ANSYS*

A pile-and-soil system similar to Test C1 was modeled using *ANSYS* (*1*) to verify the applicability and accuracy of

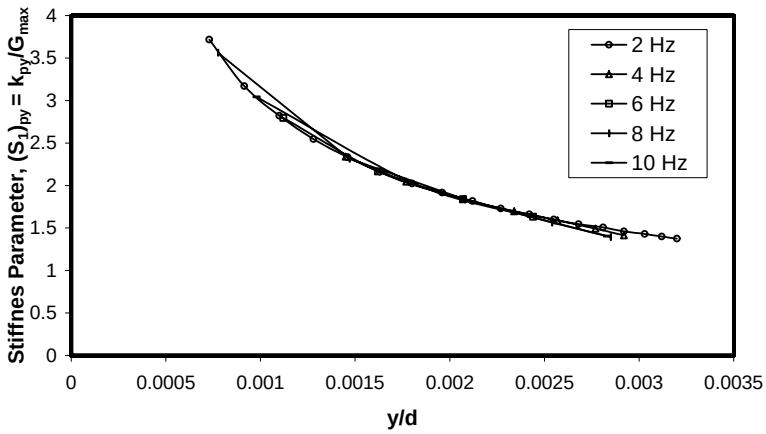

Figure B-37. True stiffness parameter for Test C1 (soft clay).

the dynamic *p-y* curve model in a standard structural analysis program. A dynamic harmonic load with peak amplitude of 100 kN at a frequency of 6 Hz was applied to the head of the same steel-pipe pile used in Test C1. The soil stiffness was modeled using three procedures: (1) static *p-y* curves; (2) dynamic *p-y* curves using Equation B-27; and (3) complex stiffness method using equivalent damping constants. The pile-head response for each test was obtained and compared with the results from the two-dimensional *p-y* curve model.

The pile was modeled using two-noded beam elements and was discretized into 10 elements that increased in length with depth. At each pile node, a spring or a spring and a dashpot were attached to both sides of the pile to represent the appropriate loading condition at the pile-soil interface. The pile and soil remained connected and had equal displacement for compressive stresses. The spring or the spring-and-dashpot model disconnects if tensile stress is detected in the soil, allowing a gap to develop.

The soil was first modeled using nonlinear springs with force displacement relationships calculated directly from static *p-y* curves. The soil stiffness was then modeled using the approximate dynamic *p-y* curve relationship calculated for Test C1 using Table B-2. The last computational test considered a spring and a dashpot in parallel.

The pile-head response for each computational test is shown in Figures B-39 and B-40, along with the calculated response from the two-dimensional analytical *p-y* model. Figure B-39a shows that the static *p-y* curves model computed larger displacements with increasing amplitudes as the number of cycles increased. Figure B-39b shows that the response computed using the dynamic *p-y* curve model was in good agreement with the response computed using the two-dimensional analytical model. The results obtained using the complex stiffness model are presented in Figure B-40a and show a decrease in displacement amplitude. The overdamped response can be attributed to using an average damping constant, which

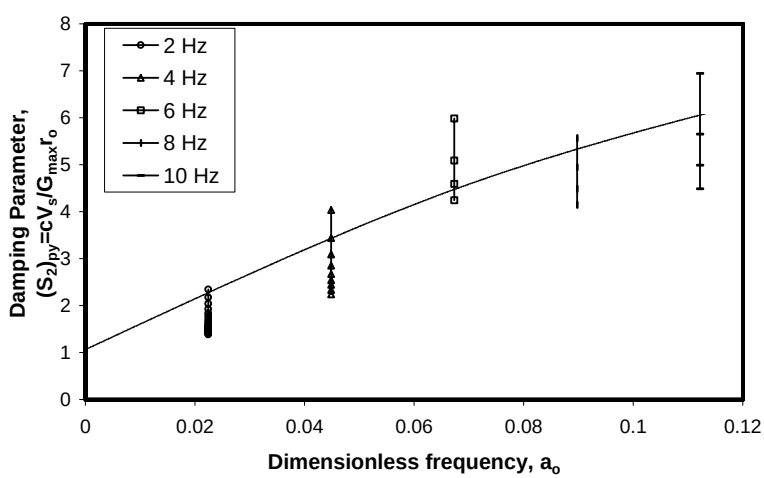

Figure B-38. Equivalent damping parameter for Test C1 (soft clay) with dimensionless frequency.

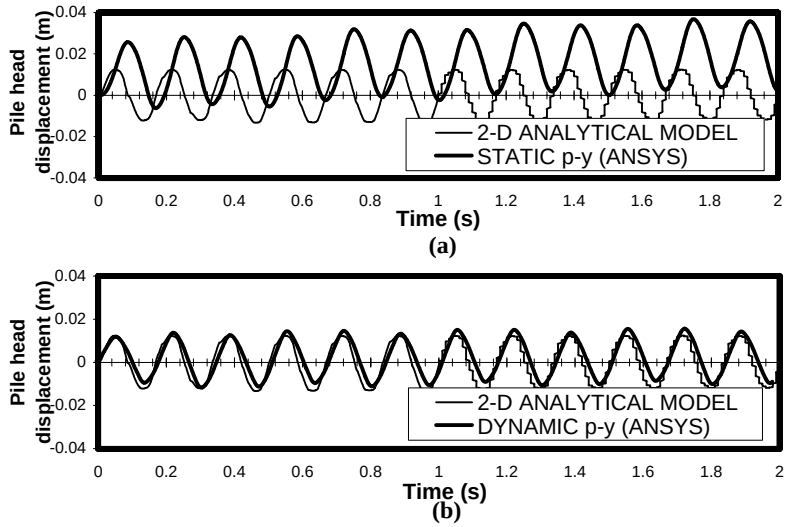

Figure B-39. Calculated pile-head response using two-dimensional analytic model compared with ANSYS using (a) static p-y *curves and (b) dynamic* p-y *curves.*

overestimates the damping at higher frequencies and large nonlinearity. Figure B-40b shows the response of the two-dimensional model compared with the complex stiffness approach with the average damping constant reduced by 50 percent. The results show that the response in this case is in good agreement with the response computed using the two-dimensional analytical model.

DYNAMIC *p*-MULTIPLIERS

One reasonable approach to account for pile-soil-pile interaction for piles in a group would be to predict the loss in soil resistance relative to that of an isolated single pile. Poulos and Davis (*9*) introduced the interaction-factors concept to reduce the soil stiffness in the context of linear elastic analysis. Focht and Koch (*39*) extended that linear elastic procedure to introduce the nonlinearity of soil into the evaluation of group interaction factors by applying a *y*-multiplier to "stretch" *p-y* curves. Cox et al. (*40*) described an alternate approach to account approximately for the group effect, in which a "*p*-factor" would be used to "shrink" the *p*-values on the *p-y* curve rather than to stretch the *y*-values.

The *p*-multiplier concept was formalized by Brown et al. (*41*) and Brown and Bollman (*42*). This concept states that lat-

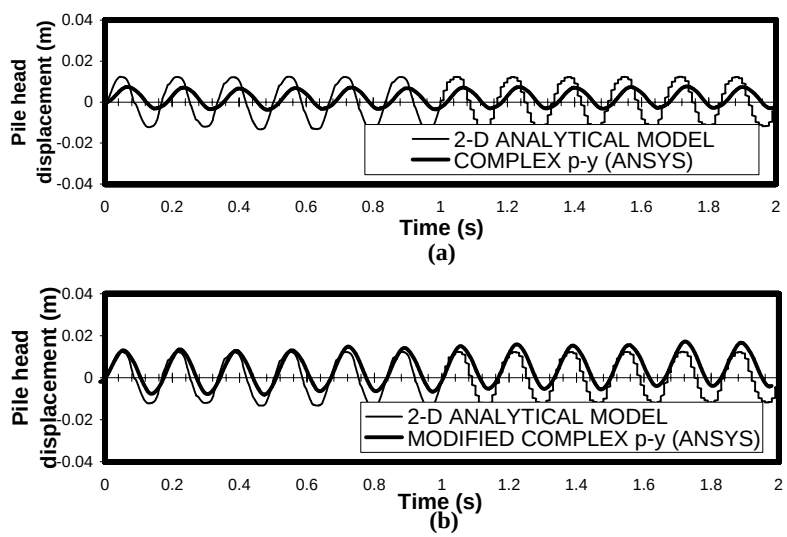

Figure B-40. Calculated pile-head response, two-dimensional analytic model, compared with ANSYS using (a) complex stiffness and (b) modified complex stiffness.

eral group action reduces the *p*-value on the *p-y* curve at every point on every *p-y* curve for a given pile (based on its geometric position in the group) by the same amount, regardless of pile deflection. In this manner, the *p*-multiplier provides a means for expressing the elastic interaction that appears in the interaction factors plus an actual reduction in ultimate soil resistance. The *p*-multiplier assumes a different value depending upon whether a pile is in a leading position or in a trailing position and the angle between the line connecting the two piles and the load direction, θ. Using the *p*-multipliers would allow the analysis of the lateral response of a pile group as an ensemble of individual piles. The soil resistance to the movement of each of these individual piles would be represented by *p-y* curves with *p*-values reduced by properly chosen *p*-multipliers. For example, the Florida Pier Program (FLPIER; see Appendix C) uses *p*-multipliers as an option for considering lateral group action. The *p*-multipliers found in the literature are given either by row (i.e., the same *p*-multiplier value for all piles in the same row) or by assuming different values for each pile. In the latter case, the total *p*-multiplier for any pile is obtained by multiplying (rather than by summing) the *p*-multipliers due to all the piles in the group.

The *p*-multipliers reported in the literature were developed from the analysis of static or cyclic load tests on single piles and pile groups. These tests, however, do not represent the dynamic loading conditions during an earthquake event; therefore, it is necessary to check the validity of the *p*-multiplier concept under dynamic loading conditions and develop, if possible, *p*-multipliers from dynamic loading events. This was a major objective of the overall project. The following section describes the results of an exploratory investigation into dynamic *p*-multipliers, independent of the analysis of the load tests conducted explicitly for this project (see Appendix D).

The approach suggested by El Naggar and Novak (*23*) to account for the group effect, along with the analytical model described above for the analysis of a single pile's response, was used to analyze the response of a single pile and groups of two piles to a prescribed harmonic displacement at the pile heads. Thus, dynamic *p*-multipliers could be established by comparing the soil resistance for a pile in a group of two piles with that of a single pile. At this point, a limited parametric study was considered for piles in cohesionless soil with different densities (e.g., loose, medium, and dense sand profiles). The parameters whose influence on *p*-multipliers is investigated in this study for a given pile-and-soil profile include

- The ratio of the spacing between the two piles to the diameter of the piles, *S/d;*
- The pile-head displacement ratio, *y/d;*
- The dimensionless frequency, a_0; and
- The angle between the line connecting the two piles and the load direction, θ.

To establish the *p*-multiplier, two loading cases were considered separately: a pile loaded individually and a group of two identical piles. In both loading cases, a prescribed harmonic displacement with specified peak amplitude was applied at the pile head, the response was analyzed, and the force at the pile head was calculated. The *p*-multiplier was approximated by the peak pile-head force at one pile in the two-pile group divided by the peak force for the single pile. The loading starts from zero, and the forces are established after five loading cycles. The response was found to stabilize almost completely after this number of cycles.

The *p*-multiplier was plotted versus the peak of the applied harmonic displacement, as a ratio of the pile diameter. Figure B-41 shows the *p*-multipliers for piles installed in loose sand (S4 in Table B-1), and θ equals 0°. It can be noted from Figure B-41 that the main factors that affect the *p*-multipliers in this case are the spacing ratio, *S/d,* and the pile-head displacement ratio, *y/d.* The *p*-multiplier increased as *S/d* increased, meaning that the group effect decreased. The *p*-multipliers also increased as the *y/d* increased. This means that during a dynamic loading event, which is characterised by large pile-head displacement, the pile-soil-pile interaction decreases, and the piles tend to behave as individual piles. This may be attributed to the concentration of soil deformations in the vicinity of the pile at higher displacements. Comparing the *p*-multipliers in Figure B-41 obtained for different loading frequencies, it can be seen that the effect of the frequency on the *p*-multipliers is small and that there is no clear trend for it.

Figures B-42 and B-43 show the *p*-multipliers for piles installed in medium-dense and dense sand, respectively. Similar observations can be made for both cases. The *p*-multipliers increased as both *S/d* and *y/d* increased, and the effect of the frequency is negligible. It must be emphasised, however, that these observations are based on limited results. Further investigations should be done before these observations can be asserted. Also, the behavior of piles in clay is different and is currently under investigation.

The *p*-multipliers shown in Figures B-42 and B-43 (and similar ones for other soil profiles) could be curve fitted. The best curve-fit function would be in the form

$$p\text{-multiplier} = f\,(S/d, y/d, a_0, \theta) \qquad \text{(B-35)}$$

This function can then be evaluated to yield the *p*-multiplier according to *S/d,* θ values for each two piles in the group, and the expected *y/d* and a_0 for a specific event.

SUMMARY, CONCLUSIONS, AND RECOMMENDATIONS FOR IMPROVEMENTS

Summary and Conclusions

A simple, two-dimensional analysis method was developed to model the response of piles to dynamic loads. The model was formulated in the time domain and developed to model transient nonlinear response of the pile-soil system efficiently. Static *p-y* curves were used to generate the nonlinear

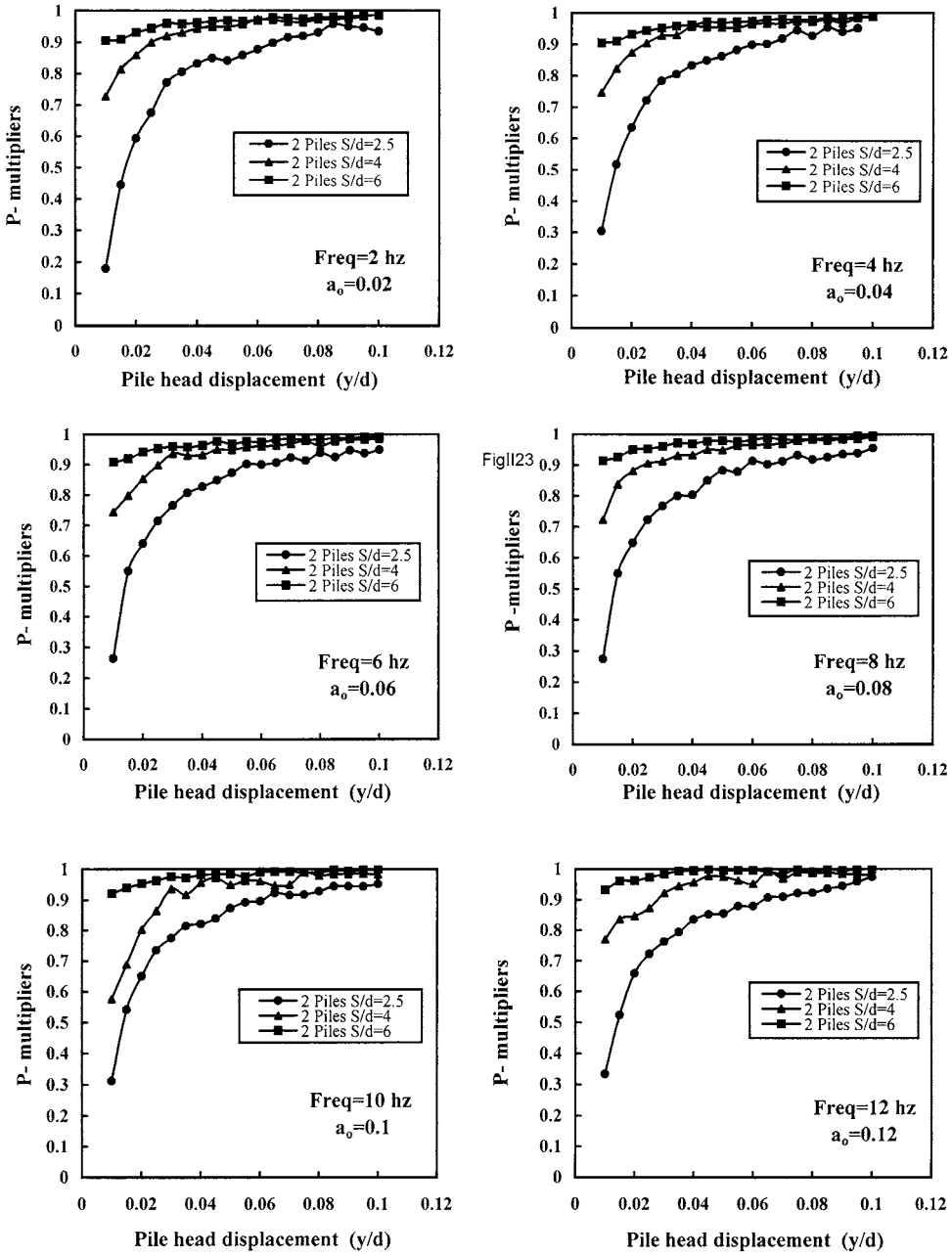

Figure B-41. p-*Multipliers versus pile-head displacement for loose sand.*

soil stiffness in the context of a Winkler model. The piles were assumed to be vertical and circular, although piles with other cross sections can be modeled by simply computing an equivalent radius r_0 for the noncircular pile. The piles were modeled using standard beam elements. A practically accurate and computationally efficient model was developed to represent the soil reactions. This model accounted for soil nonlinearity, slippage and gapping at the pile-soil interface, and viscous and material damping.

Dynamic soil reactions (dynamic *p-y* curves) were generated for a range of soil types and harmonic loading with varying frequencies applied at the pile head. Closed-form solutions were derived from regression analysis relating the static *p-y* curve, dimensionless frequency, and apparent velocity of the soil particles. That model is summarized in Equation B-27, which converts a static *p-y* model into an approximate dynamic model by multiplying *p*-values on the static *p-y* curve (such as the API sand curve) by a factor that is dependent upon both frequency and lateral pile displacement relative to the pile diameter. Several curve-fitting parameters that were necessary to write Equation B-27 in closed form from the results of numerous numerical solutions are given in Table B-2.

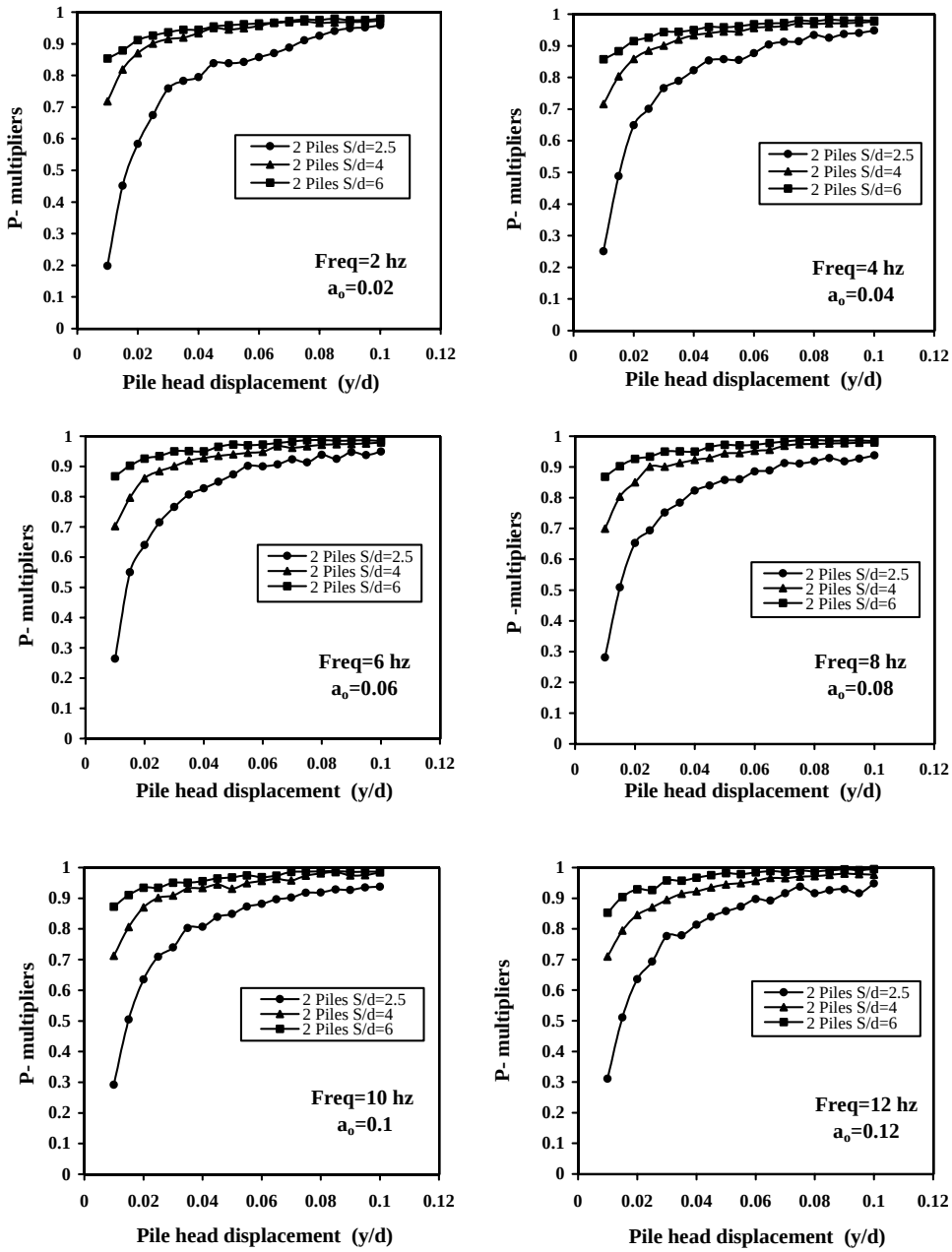

Figure B-42. p-*Multipliers versus pile-head displacement for medium-dense sand.*

Although the dynamic *p-y* curves are frequency dependent, they are approximately frequency independent for frequencies above about 10 Hz (ω = 62.8 radians). This model is included in FLPIER (see Appendix C), although verification against full-scale or centrifuge tests on piles using this relationship was not accomplished with FLPIER within the time-frame limitations of this project.

A simple spring-and-dashpot model was also proposed whose constants were established by splitting the dynamic *p-y* curves into real (stiffness) and imaginary (damping) components. The model is summarized in Equation B-29, in which a displacement-dependent soil stiffness, *k*, is determined from Equation B-31 and displacement- and frequency-dependent damping is determined from Equation B-32. This model appears to be most accurate for dimensionless frequencies ($a_0 = \omega r_0/V_s$) > 0.02. This model is intended to be used in programs that employ equivalent linear analyses for harmonic loading at the pile head.

The proposed dynamic *p-y* curves and the spring-and-dashpot model were incorporated into a commercial finite element program (ANSYS) that was used to compute the response of a laterally loaded pile. The computed responses

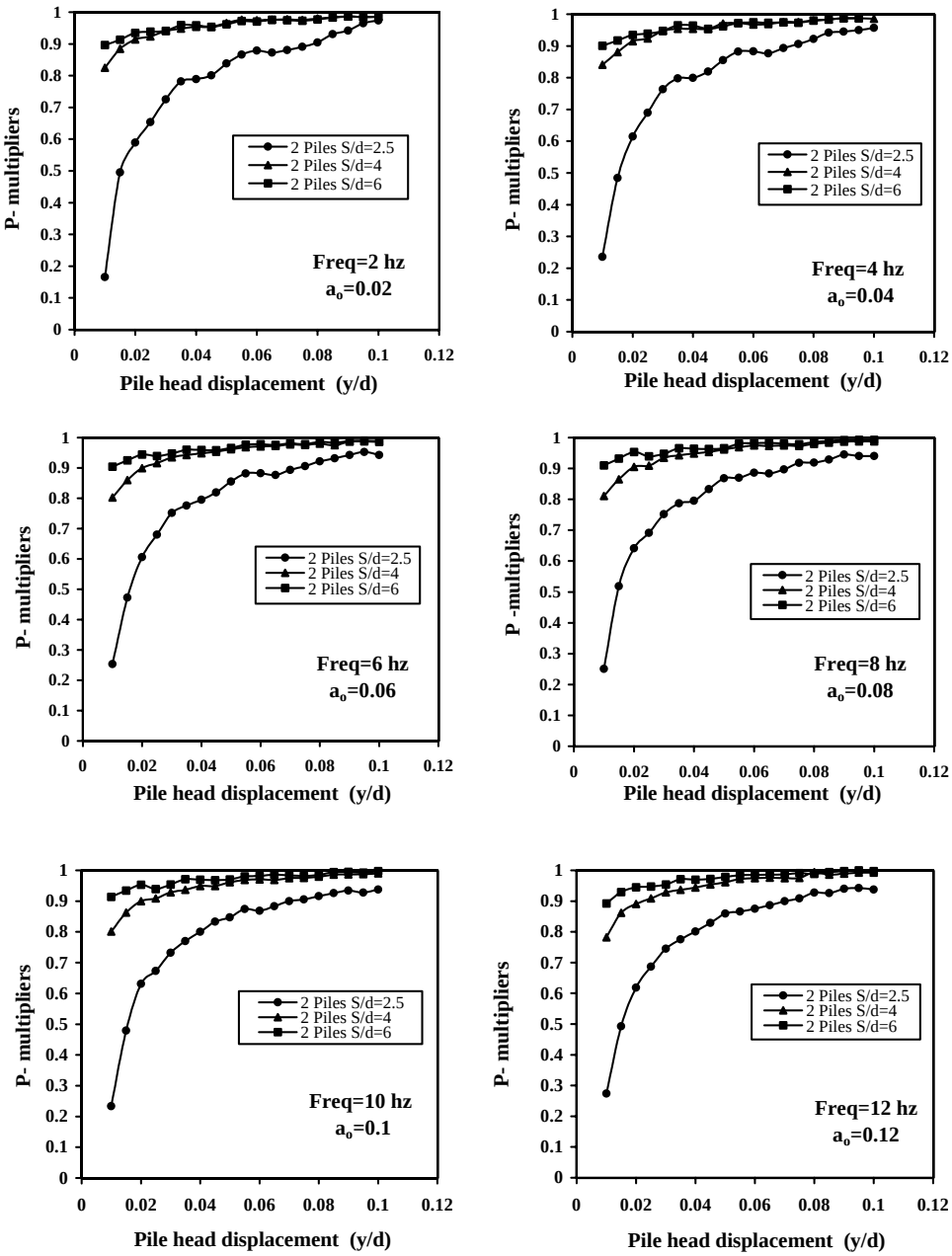

Figure B-43. p-*Multipliers versus pile-head displacement for dense sand.*

compared well with the predictions of the two-dimensional analysis.

The group effect (lateral pile-soil-pile interaction through the soil) was considered in the analysis, and a procedure for the development of dynamic *p*-multipliers for sand profiles was proposed. Like the *p-y* curves, the *p*-multipliers are frequency dependent; however, based on limited evidence given herein (see Figures B-41 through B-43), the *p*-multipliers for loose through dense sand can be treated in design practice as frequency independent in the frequency range $a_0 = \omega r_0 / V_s = 0.02$ to 0.12, especially for pile-head displacements (y) equal to or greater than 0.2 d, where d is the pile diameter (or equivalent diameter for noncircular piles). Such displacements are typical of those for which solutions are needed for extreme-event loading.

For relatively low frequencies, the predominant frequency of the earthquake motion being modeled can be used to compute the values on the *p-y* curves. However, for cases in which inertial behavior is stronger than kinematic behavior (the piles are driven by inertial superstructure feedback rather than the kinematic motion of the surrounding soil), the natural frequency of the structure being modeled may be the controlling predominant frequency, ω, to be used in evaluating the dynamic *p-y* curves and *p*-multipliers. Selec-

tion of a value for ω must therefore be done carefully by the user of the model (Equations B-27, B-29, B-30, and B-32). If the user decides that the primary frequency at the pile head will be 10 Hz or greater, the *p-y* model can be evaluated by setting $\omega = 62.8$ radians/s in the expression for a_0, and the curve can be treated as frequency independent.

The dynamic *p-y* curves and the dynamic *p*-multipliers can then be used to model the dynamic lateral behavior of pile groups approximately, either in FLPIER or in other software that uses *p-y* models for the soil.

Recommendations for Further Development

The dynamic *p*-multipliers have been developed exclusively for sand profiles (in which strength and stiffness increase with depth). Time and resources did not permit a corresponding development for clay profiles. Further development of the model should include the development of *p*-multipliers for clay profiles (uniform strength stiffness with depth) and for mixed soil profiles. The model should also be used directly in FLPIER (see Appendix C) to ensure that it is performing properly in the context of that computer code.

REFERENCES—APPENDIX B

1. *General Finite Element Analysis Program,* Version 5.4. ANSYS, Inc. (1996).
2. Wu, G., and W. D. L. Finn. "Dynamic Nonlinear Analysis of Pile Foundations Using Finite Element Method in the Time Domain," *Canadian Geotechnical Journal,* Vol. 34 (1996); pp. 44–52.
3. Trochanis, A. M., J. Bielak, and P. Christiano. "A Three-Dimensional Nonlinear Study of Piles Leading to the Development of a Simplified Model," Technical Report National Science Foundation Grant No. ECE-86/1060, Carnegie Mellon University (1988).
4. "Recommended Practice for Planning, Designing and Constructing Fixed Offshore Platforms," *API Recommended Practice 2A* (19th edition). American Petroleum Institute (1991); pp. 47–55.
5. Novak, M., and H. Mitwally. "Transmitting Boundary for Axisymmetrical Dilation Problems." *Journal of Engineering Mechanics,* ASCE, Vol. 114, No. 1, (1988); pp. 181–187.
6. National Center for Earthquake Engineering Research Information Service, State University of New York at Buffalo website: nceer.eng.buffalo.edu (1998).
7. Kramer, S. L. *Geotechnical Earthquake Engineering.* Prentice-Hall (1996).
8. El Sharnouby, B., and M. Novak. "Static and Low Frequency Response of Pile Groups," *Canadian Geotechnical Journal,* Vol. 22, No. 2 (1985); pp. 79–84.
9. Poulos, H. G., and E. H. Davis. *Pile Foundation Analysis and Design.* John Wiley and Sons (1980).
10. Idriss, I. M., and J. I. Sun. "Modifications to SHAKE Program Published in Dec. 1972 by Schnabel, Lysmer & Seed," *User's Manual for SHAKE91* (with Accompanying Program), Center for Geotechnical Modeling, University of California at Berkeley (1992).
11. Takemiya, H., and Y. Yamada. "Layered Soil-Pile-Structure Interaction," *Earthquake Engineering and Structural Dynamics,* Vol. 9 (1981); pp. 437–457.
12. Flores-Berrones, R., and R. V. Whitman. "Seismic Responses of End-Bearing Piles," *Journal of Geotechnical Engineering,* ASCE, Vol. 108 (1982); pp. 555–569.
13. Gazetas, G. "Seismic Response of End-Bearing Piles," *International Journal of Soil Dynamics and Earthquake Engineering,* Vol. 3, No. 2 (1984); pp. 82–93.
14. Tazoh, T., T. Wakahara, and K. Shimizu. "Effective Motion of Group Pile Foundation," *Proceedings, 9th World Conference on Earthquake Engineering,* Vol. III (1988).
15. Ahmad, S., and S. M. Mamoon. "Seismic Response of Floating Piles to Obliquely Incident Waves," *Proceedings, 2nd International Conference on Recent Advances in Geotechnical Earthquake Engineering and Soil Dynamics,* Vol. I, St. Louis, MO (1991); pp. 805–813.
16. Fan, K., G. Gazetas, A. Kaynia, E. Kausel, and S. Ahmad. "Kinematic Seismic Response of Single Piles and Pile Groups," *Journal of Geotechnical Engineering,* ASCE, Vol. 117, No. 12, (1991); pp. 1860–1879.
17. Kaynia, A. M., and E. Kausel. "Dynamic Stiffnesses and Seismic Response of Pile Groups," *Research Report.* Massachusetts Institute of Technology (1982).
18. Makris, N., and G. Gazetas. "Dynamic Pile-Soil-Pile Interaction, Part II: Lateral and Seismic Response," *Earthquake Engineering and Structural Dynamics,* Vol. 21 (1992); pp. 145–162.
19. Novak, M., T. Nogami, and F. Aboul-Ella. "Dynamic Soil Reactions for Plane Strain Case," *Journal of the Engineering Mechanics Division,* ASCE, Vol. 104 (1978); pp. 953–959.
20. Gazetas, G., and R. Dobry. "Horizontal Response of Piles in Layered Soils," *Journal of Geotechnical Engineering,* ASCE, Vol. 110, No. 1 (1984); pp. 20–40.
21. Nogami, T., K. Konagai, J. Otani, and H. L. Chen. "Nonlinear Soil-Pile Interaction Model for Dynamic Lateral Motion," *Journal of Geotechnical Engineering,* ASCE, Vol. 118, No. 1 (1992); pp. 106–116.
22. El Naggar, M. H., and M. Novak. "Nonlinear Lateral Interaction in Pile Dynamics," *Journal of Soil Dynamics and Earthquake Engineering,* Vol. 14, No. 3 (1995); pp. 141–157.
23. El Naggar, M. H., and M. Novak. "Nonlinear Analysis for Dynamic Lateral Pile Response," *Journal of Soil Dynamics and Earthquake Engineering,* Vol. 15, No. 4 (1996); pp. 233–244.
24. Novak, M., and M. Sheta. "Dynamic Response of Piles and Pile Groups," *Proceedings, 2nd International Conference on Numerical Methods in Offshore Piling,* Austin (1982); pp. 489–507.
25. Hardin, B. O., and W. L. Black. "Vibration Modulus of Normally Consolidated Clay," *Journal of the Soil Mechanics and Foundations Division,* ASCE, Vol. 94, No. SM2 (1968); pp. 353–369.
26. Matlock, H. "Correlations for Design of Laterally Loaded Piles in Soft Clay," *Proceedings, 2nd Offshore Technology Conference,* Vol. 1, Houston (1970); pp. 577–588.
27. Bhushan, K., S. C. Haley, and P. T. Fong. "Lateral Load Tests on Drilled Piers in Stiff Clays," *Journal of the Geotechnical Engineering Division,* ASCE, Vol. 105, No. GT8 (1979); pp. 969–985.

28. Reese, L. C., and R. C. Welch. "Lateral Loading of Deep Foundations in Stiff Clay," *Journal of the Geotechnical Engineering Division*, ASCE, Vol. 101, No. GT7 (1975); pp. 633–649.
29. Reese, L. C., W. R. Cox, and F. D. Koop. "Field Testing and Analysis of Laterally Loaded Piles in Stiff Clay," *Proceedings, 7th Annual Offshore Technology Conference*, Vol. 2, Houston (1975); pp. 671–690.
30. Desai, C. S., and T. H. Wu. "A General Function for Stress-Strain Curves," *Proceedings, 2nd International Conference on Numerical Methods in Geomechanics*, ASCE, Vol. 1 (1976); pp. 306–318.
31. Abendroth, R. E., and L. F. Greimann. "Pile Behavior Established from Model Tests" *Journal of Geotechnical Engineering*, ASCE, Vol. 116, No. 4 (1990); pp. 571–588.
32. Reese, L. C., W. R. Cox, and F. D. Koop. "Analysis of Laterally Loaded Piles in Sand," *Proceedings, 6th Annual Offshore Technology Conference*, Vol. 2, Houston (1974); pp. 473–483.
33. Bhushan, K., L. J. Lee, and D. B. Grime. "Lateral Load Tests on Drilled Piers in Sand," *Drilled Piers and Caissons*, M. W. O'Neill (ed.); ASCE (1981); pp. 131–143.
34. Bhushan, K., and S. Askari. "Lateral Load Tests on Drilled Pier Foundations for Solar Plant Heliostats" Laterally Loaded Piles, *ASTM STP 835*, J. A. Langer (ed.), ASTM (1984); pp. 141–155.
35. Bhushan, K., and S. C. Haley. "Development of Computer Program Using P-Y Data from Load Test Results for Lateral Load Design of Drilled Piers," Research report prepared for Woodward-Clyde Consultants Professional Development Committee (1980).
36. Meyer, B. J., and L. C. Reese. "Analysis of Single Piles Under Lateral Loading" *Research Report 244-1*, Center for Highway Research, University of Texas at Austin (1979) pp. 1–145.
37. Idriss, I. M., R. Dobry, and R. D. Singh. "Nonlinear Behavior of Soft Clays During Cyclic Loading," *Journal of the Geotechnical Engineering Division*, ASCE, Vol. 104, No. GT12 (1978); pp. 1427–1447.
38. El Naggar, M. H. "Interpretation of Lateral Statnamic Load Test Results" *Geotechnical Testing Journal*, ASTM, Vol. 21, No. 3 (1998); pp. 169–179.
39. Focht, J. A., Jr., and K. J. Koch. "Rational Analysis of the Lateral Performance of Offshore Pile Groups," *Proceedings, Offshore Technology Conference*, Dallas (1973).
40. Cox, W. R., D. A. Dixon, and B. S. Murphy. "Lateral Load Tests on 25.4-mm (1-in.) Diameter Piles in Very Soft Clay in Side-by-Side and In-Line Groups," *STP 835*, ASTM (1984); pp. 122–139.
41. Brown, D. A., C. Morrison, and L. C. Reese. "Lateral Load Behaviour of Pile Group in Sand," *Journal of Geotechnical Engineering*, ASCE, Vol. 114, No. 11 (1988); pp. 1326–1343.
42. Brown, D. A., and H. Bollman. "Pile Group Design for Lateral Loading Using COM 624," *Proceedings, Conference on the Design of Bridges for Extreme Events*, U.S. DOT, FHWA (1996).

APPENDIXES C THROUGH F

UNPUBLISHED MATERIAL

Appendixes C through F contained in the research agency's final report are not published herein. For a limited time, loan copies are available on request to NCHRP, Transportation Research Board, Box 289, Washington, D.C., 20055. The appendixes are titled as follows:

- Appendix C: Dynamic Model for Laterally Loaded Pile Groups—Computational Model (FLPIER);
- Appendix D: Testing at Wilmington, North Carolina;
- Appendix E: Testing at Spring Villa NGES, Alabama; and
- Appendix F: Calibration of Strain Gauges and Correction of Raw Strain Data.

The **Transportation Research Board** is a unit of the National Research Council, which serves the National Academy of Sciences and the National Academy of Engineering. The Board's mission is to promote innovation and progress in transportation by stimulating and conducting research, facilitating the dissemination of information, and encouraging the implementation of research results. The Board's varied activities annually draw on approximately 4,000 engineers, scientists, and other transportation researchers and practitioners from the public and private sectors and academia, all of whom contribute their expertise in the public interest. The program is supported by state transportation departments, federal agencies including the component administrations of the U.S. Department of Transportation, and other organizations and individuals interested in the development of transportation.

The National Academy of Sciences is a private, nonprofit, self-perpetuating society of distinguished scholars engaged in scientific and engineering research, dedicated to the furtherance of science and technology and to their use for the general welfare. Upon the authority of the charter granted to it by the Congress in 1863, the Academy has a mandate that requires it to advise the federal government on scientific and technical matters. Dr. Bruce M. Alberts is president of the National Academy of Sciences.

The National Academy of Engineering was established in 1964, under the charter of the National Academy of Sciences, as a parallel organization of outstanding engineers. It is autonomous in its administration and in the selection of its members, sharing with the National Academy of Sciences the responsibility for advising the federal government. The National Academy of Engineering also sponsors engineering programs aimed at meeting national needs, encourages education and research, and recognizes the superior achievements of engineers. Dr. William A. Wulf is president of the National Academy of Engineering.

The Institute of Medicine was established in 1970 by the National Academy of Sciences to secure the services of eminent members of appropriate professions in the examination of policy matters pertaining to the health of the public. The Institute acts under the responsibility given to the National Academy of Sciences by its congressional charter to be an adviser to the federal government and, upon its own initiative, to identify issues of medical care, research, and education. Dr. Kenneth I. Shine is president of the Institute of Medicine.

The National Research Council was organized by the National Academy of Sciences in 1916 to associate the broad community of science and technology with the Academy's purpose of furthering knowledge and advising the federal government. Functioning in accordance with general policies determined by the Academy, the Council has become the principal operating agency of both the National Academy of Sciences and the National Academy of Engineering in providing services to the government, the public, and the scientific and engineering communities. The Council is administered jointly by both the Academies and the Institute of Medicine. Dr. Bruce M. Alberts and Dr. William A. Wulf are chairman and vice chairman, respectively, of the National Research Council.

Abbreviations used without definitions in TRB publications:

AASHO	American Association of State Highway Officials
AASHTO	American Association of State Highway and Transportation Officials
ASCE	American Society of Civil Engineers
ASME	American Society of Mechanical Engineers
ASTM	American Society for Testing and Materials
FAA	Federal Aviation Administration
FHWA	Federal Highway Administration
FRA	Federal Railroad Administration
FTA	Federal Transit Administration
IEEE	Institute of Electrical and Electronics Engineers
ITE	Institute of Transportation Engineers
NCHRP	National Cooperative Highway Research Program
NCTRP	National Cooperative Transit Research and Development Program
NHTSA	National Highway Traffic Safety Administration
SAE	Society of Automotive Engineers
TCRP	Transit Cooperative Research Program
TRB	Transportation Research Board
U.S.DOT	United States Department of Transportation

THE NATIONAL ACADEMIES

Advisers to the Nation on Science, Engineering, and Medicine

National Academy of Sciences
National Academy of Engineering
Institute of Medicine
National Research Council